ATOMIC, ELECTRONIC, AND TRANSPORT PROPERTIES OF QUANTUM POINT CONTACTS ON GRAPHITE SURFACE

A THESIS

SUBMITTED TO THE DEPARTMENT OF PHYSICS

AND THE INSTITUTE OF ENGINEERING AND SCIENCE

OF BILKENT UNIVERSITY

IN PARTIAL FULFILLMENT OF THE REQUIREMENTS

FOR THE DEGREE OF

MASTER OF SCIENCE

By

Çetin Kılıç

September 1997

ATOMIC, ELECTRONIC, AND TRANSPORT PROPERTIES OF QUANTUM POINT CONTACTS ON GRAPHITE SURFACE

A THESIS

SUBMITTED TO THE DEPARTMENT OF PHYSICS

AND THE INSTITUTE OF ENGINEERING AND SCIENCE

OF BILKENT UNIVERSITY

IN PARTIAL FULFILLMENT OF THE REQUIREMENTS

FOR THE DEGREE OF
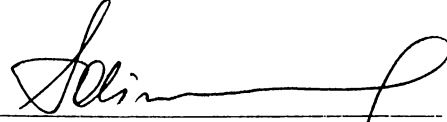
MASTER OF SCIENCE

By

Çetin Kılıç

September 1997

I certify that I have read this thesis and that in my opinion it is fully adequate, in scope and in quality, as a dissertation for the degree of Master of Science.

Prof. Salim Çiraci (Supervisor)
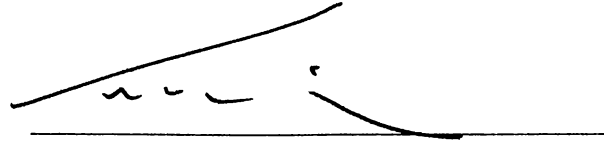
I certify that I have read this thesis and that in my opinion it is fully adequate, in scope and in quality, as a dissertation for the degree of Master of Science.

Prof. Atilla Erçelebi

I certify that I have read this thesis and that in my opinion it is fully adequate, in scope and in quality, as a dissertation for the degree of Master of Science.

Assoc. Prof. Recai Ellialtıoğlu

Approved for the Institute of Engineering and Science:

Prof. Mehmet Baray,
Director of Institute of Engineering and Science

Abstract

ATOMIC, ELECTRONIC, AND TRANSPORT PROPERTIES OF QUANTUM POINT CONTACTS ON GRAPHITE SURFACE

Çetin Kılıç
M. S. in Physics

Supervisor: Prof. Salim Ciraci

September 1997

In this thesis, the variation of conductance through a contact formed by a hard STM tip pressing to a graphite substrate is investigated. Our study involves the molecular dynamics simulations to reveal the evolution of the atomic structure during the growth of the contact, and *ab initio* electronic structure calculations of graphite that is under the expansive and compressive strain along the [0001] axis. Combining the results obtained from these calculations, we propose a mechanism to explain the peculiar variation of the conductance. Owing to the layered structure of graphite, the variation of conductance exhibits dramatic differences from those of normal metals. It is predicted that in graphite, the conductance first increases, and then, drops to a lower value with the puncture of the atomic plane. This phenomenon repeats quasi-periodically as the tip continues to press on the surface.

Keywords: Graphite, ballistic electron transport, quantum point contact, molecular dynamics simulations, band structure calculations

Özet

GRAFİT YÜZEYİNDEKİ NOKTASAL KUVANTUM DEĞMELERİNİN ATOMİK, ELEKTRONİK VE NAKİL ÖZELLİKLERİ

Çetin Kılıç

Fizik Yüksek Lisans

Tez Yöneticisi: Prof. Salim Çiraci

Eylül 1997

Bu tezde grafit yüzeyine bastırılan sert STM tipinin oluşturduğu değmede iletkenliğin değişimi incelendi. Çalışmamızda, atomik yapının değmenin büyüme evresinde analiz edilmesi için, moleküler dinamik simülasyonları ve basma ve çekme gerilimi altında grafitin temel prensiplere dayalı elektronik yapı hesapları yapıldı. Bu hesaplardan elde edilen sonuçları birleştirerek grafit değmesinin iletkenliğinin değişimini incelemek üzere bir mekanizma önerdik. Grafitin katmanlı yapısından dolayı elektrik iletkenliğinin değme alanı ile değişimi normal metallere nazaran çok farklılıklar göstermektedir. Grafitte iletkenliğin önce artacağı, daha sonra bir tabakanın tip tarafından delinmesi sonucu düşeceği ve tipin grafiti bastırması sürerken bu olayın periyodik olarak cereyan edeceği öngörüldü.

Anahtar sözcükler: Grafit, balistic elektron nakli, noktasal kuvantum değme, moleküler dinamik simülasyonları, band yapısı hesapları

i

Acknowledgement

Contents

List of Figures

List of Tables

Chapter 1

INTRODUCTION

Atomic size contacts created by a sharp metal tip on the sample surface has been a subject of interest in recent years. In the beginning, the contact has radius of 2-4 Å , but it grows by pushing the tip further towards the sample. For metallic electron densities the contact diameter ($2R_\rho$ = 2-4 Å) is in the range of Fermi wavelength λ_F. In this length scale the level spacing of electrons transversally confined to the contact is approximately 1 eV. Moreover, the discrete structure of the contact made by atoms becomes pronounced; any change in atomic arrangement and size of the contact can lead to observable variations in mechanical and electronic properties. In particular, the two-terminal conductance G of a contact has shown discontinuous (sudden) variations while the tip is pushed continuously.[1-4] Similar behavior has been obtained recently in a connective neck that was formed by retracting the tip subsequent to a nanoindentation.[5-7] As far as the conductance is concerned, an atomic size contact or a connective neck is considered as a constriction with length l smaller than the electron mean free path l_e, and with $2R_\rho \sim \lambda_F$. Whether the two terminal ballistic conductance of such a constriction is quantized has been a subject of controversy.[8,9] While abrupt jumps or falls in the variation of conductance are attributed to the discontinuous change in the cross-section of the contact,[1,3,4] several studies favored the quantization.[5-9]

The point contact spectroscopy has been used earlier to investigate the electron-phonon interaction. The electron transport through a point contact is

important not only for a better understanding of mesoscopic physics, but also for novel device applications. Moreover, various yielding mechanics and resulting atomic rearrangements during the evolution of the contact have been active subject of study. In particular, the question whether the continuum mechanics can be applied for the formalism of the contacts is under intensive study.

Almost three decades ago, Sharvin[10] investigated the point contact with $l \sim 0$ by using a semiclassical approach, and showed that the conductance is independent of any material properties, but solely determined by the geometry (or cross-section S) of the point contact and mean electron density, $\bar{\rho}$ of the reservoir. The expression of contact conductance he obtained (which is known as the Sharvin's conductance) is given by

$$G_S = \frac{2e^2}{h} \frac{k_F^2}{4\pi} S = \frac{2e^2}{h} \left(\frac{\pi R_\rho}{\lambda_F} \right)^2 \tag{1.1}$$

According to Sharvin, G_S increases linearly with S even if S is much smaller than λ_F^2. This is, of course, against the uncertainty principle. In the quantum regime that is valid for very small S, $G_S = 0$ as long as $S < S_c$; the threshold cross-section S_c is fixed by the uncertainty principles. Therefore, in the quantum regime G_S deviates from the above expression. A realistic atomic-size contact has finite length ($l \neq 0$), and hence its conductance variation differs from the semiclassical Sharvin's conductance.

Ciraci and Tekman[3] developed the first quantum theory for the conductance of a three-dimensional (3D) point contact as a function of l. They found that for a uniform and very long ($l \gg \lambda_F$) contact G(S) exhibits sharp step structure having step heights at integer multiples of $2e^2/h$. This stepped structure is smeared out if $l < \lambda_F$. They attributed the observed sudden changes in the experimental $G(S)$ curve to the sudden (discrete) changes in S under the compressive stress. Recent experiments[6] measuring force and conductance simultaneously, and the results of simulations based on molecular dynamics calculations[4] appear to confirm this theory. Several recent studies on the atomic size contacts and connective necks have contributed significantly to our understanding of the ballistic conductance in metal contacts. A summary of the recent understanding on the quantization

of ballistic conductance is presented here. By considering the contact as a constriction between two electron reservoirs, the electronic states are transversally confined in 2D, but propagate along the third direction. The states (with corresponding eigenenergies) in the constriction are expressed as

$$\psi_{ij\gamma} = \varphi_{ij}e^{i\gamma z}, \quad E_{ij\gamma} = \epsilon_{ij} + \frac{\hbar^2\gamma^2}{2m} \tag{1.2}$$

An electron entering the constriction evolves into a current transporting state with proper energy and momentum conservations. Such a state can be expressed as a linear combination of $\psi_{ij\gamma}$. For a uniform constriction with l smaller than the mean free path l_e but $l > \lambda_F$, each current transporting state (having degeneracy n_{ij}) with $E_F < E_{ij\gamma} < E_F + eV$ (V being the bias voltage) can contribute to the conductance by $2n_{ij}e^2/h$. Therefore, a uniform and ideal constriction would have $G(S)$ curve that displays the staircase structure with sharp steps. However, when $l < \lambda_F$ and atomic structure is irregular; the true $G(S)$ curve normally increases with S, but is smeared out and exhibits sudden changes whenever S has a discontinuous growth. The variation of G with S for a contact between metal tip and sample surface demonstrates the quantization of electronic states in the constriction, but not the quantization of ballistic conductance.

The conductance of the point contact generated by sharp tip on the graphite is found rather peculiar and different from the above picture. In the experiments done at Bilkent,[11] and IBM Zürich Laboratory,[12] it is found that $G(s)$ does not increase with the push of the tip s, but oscillates between two values. So far no understanding has developed for such a behavior, and hence the conductance of the contact formed on the graphite surface has remained a mystery. Graphite has very interesting and directional properties[13,14]; it is an important material for STM[15] and intercalation process.[13] In addition, graphite is essential for carbon bucky-balls (fullerenes) and nanotubes. Carbon-carbon bonds are very strong within a layer, but interlayer interaction is very weak. This anisotropy leads to a very soft Young modulus E, and very small conductance G ($\sim 1 \ \Omega^{-1}cm$) along the direction perpendicular to the layers, whereas in layers G ($\sim 1 \times 10^4 \ \Omega^{-1}cm$) can have metallic values.[13] Moreover, graphitic planes are rather inert due to

strong covalent bonds of which they are made up. The directional behavior is also reflected to the electronic structure making graphite a semimetal with a very narrow Fermi surface.

The strange behavior of the atomic size contact on graphite surface is important for mesoscopic physics, and is investigated in this thesis. This study involves state-of-the-art molecular dynamics simulations and *ab initio* total energy, band, and density of states calculations. The results of energy band calculations yield semimetal to metal transition under uniaxial compression. The indentation of a sharp and hard tip on the graphite surface proceeds discontinuously each time making a puncture on a new graphite layer. Based on these results, we propose a model that successfully explains the peculiar behavior of electron transport through an atomic contact created by an STM tip. Besides, the mechanism revealed in this study can lead to potential device applications.

Chapter 2

TRANSPORT IN SCANNING TUNNELING MICROSCOPY

2.1 Transition to Quantum Point Contact

Scanning tunneling microscopy (STM) was the first technique which gives the possibility of direct probing of surface structure in real-space, ultimately with atomic resolution. A point-like probe (being kept proximate to the surface) is combined with a piezoelectric drive system to scan the sample, providing local information via vacuum tunneling of electrons. Scanning is performed by several modes operating the tip. Among all, the constant current mode is most commonly used.[15] In this mode, in order to keep the tunneling current constant, a feedback circuit adjusts the tip height z by applying an appropriate voltage V_z to the z piezoelectric drive. The lateral tip position (x, y) is determined by the values V_x and V_y applied to x and y piezoelectric drives, respectively. V_z is recorded with respect to the variations of V_x and V_y, and $V_z(V_x, V_y)$ is translated into $z(x, y)$ giving the topographic image of the surface.

The tip position can correspond to three different regimes[16,17] depending upon the tip-surface separation s as described in the following subsections. The first two are included since they occur prior to the point contact as s gets smaller.

2.1.1 Nearly independent electrode regime

At large separations ($s \geq 7$ Å), only weak perturbations occur within the proximity of the tip and the sample so that the energy eigenstates remain almost unaffected. The transport is via tunneling between almost unperturbed states of two electrodes. The tip and the sample are then considered nearly independent. The tunneling current I by first-order perturbation theory is[17]

$$I = \frac{2\pi e}{\hbar} \sum_{t,s} \{f(E_t)[1-f(E_s+eV)] - f(E_s+eV)[1-f(E_t)]\}|M_{ts}|^2\delta(E_s-E_t), \quad (2.1)$$

where $f(E)$ is the Fermi function, V is the applied bias voltage, M_{ts} is the tunneling matrix element between the unperturbed electronic states ψ_t of the tip and ψ_s of the sample surface with energies E_t and E_s, respectively, in the absence of tunneling. In Bardeen's transfer Hamiltonian approach[18] the tunneling matrix element is given by

$$M_{ts} = -\frac{\hbar^2}{2m} \int d\mathbf{S}(\psi_t^* \nabla \psi_s - \psi_s \nabla \psi_t^*) \quad (2.2)$$

where the integral has to be evaluated over any surface lying entirely within the vacuum barrier region between the tip and the sample.

Applying the formulation above, Tersoff and Hamann[19] calculated I considering an effective, locally spherical symmetric tip with radius of curvature R. In the limits of low temperature and small applied bias voltage, they obtained

$$I \propto e^{2\kappa R}n_t(E_F)n_s(E_F, \mathbf{r}_t) \quad (2.3)$$

within s-wave approximation for the tip. The decay rate κ is proportional the effective local potential barrier height ϕ as expressed by Eqn. (2.5) below. $n_t(E_F)$ denotes the density of states (DOS) of the tip at the Fermi level.

$$n_s(E_F, \mathbf{r}_t) = \sum_s |\psi_s(\mathbf{r}_t)|^2\delta(E_s - E_F) \quad (2.4)$$

is the surface local density of states (LDOS) at the Fermi level evaluated at the center of curvature $\mathbf{r}_t$ of the tip. Moreover, the surface wave functions decay exponentially in the direction normal to the surface through the barrier.

Therefore, dependence of the tunneling current I and the tunneling conductance G (derived from I) on the separation distance s is also exponential:

$$I \propto e^{-2\kappa s} \; ; \qquad \kappa = \frac{\sqrt{2m\phi}}{\hbar} \tag{2.5}$$

This expression is an approximation for certain special cases. In this form, the p_z and d orbital contribution of tip states, the tip-sample interactions, and the detailed variation of $\phi(z)$ are not taken into account.

The Apparent Barrier Height

Tersoff and Hamann[19] assumed the potential barrier ϕ to be laterally uniform and equal to the surface work function ϕ_s, *i.e.* the work needed to remove an electron from the Fermi level to vacuum, or practically to a position outside the surface. However, to generalize, an apparent local barrier height is determined by measuring the slope of $\ln I$ versus s curve at a fixed sample bias voltage V and at a fixed sample surface location.

$$\phi_A = \frac{\hbar^2}{8m} (\frac{d \ln I}{ds})^2 \tag{2.6}$$

as deduced from Eqn. (2.5).

The apparent barrier height ϕ_A increases by the influence of the band structure of materials, especially semiconductors and semimetals. Within the effective mass approximation

$$\phi_A = \phi + \frac{\hbar^2}{2m} k_{\parallel}^2, \tag{2.7}$$

where $k_{\parallel}$ is the parallel component of the wave vector to the surface.[17]

2.1.2 Electronic contact regime

As the tip approaches the sample ($s \leq 4$ Å), the electronic charge is rearranged and the ions are displaced to attain the lowest total energy. The states of the tip and the sample are combined to yield site-specific tip-induced localized states[16] (TILS) with a net binding interaction (associated with a charge accumulation

between the tip and the nearest surface atom). The tunneling current I deviates from the proportionality of LDOS. It is found that the tunneling current and the corrugation amplitude in STM is enhanced (over LDOS) by tip-induced modifications on the electronic structure within the generalization of Tersoff-Hamann theory.[16]

The tunneling gap between the tip and the sample can be viewed as a 3D constriction. In this constriction, the energy E_1 of the lowest propagating state may occur above Fermi level E_F because of the lateral confinement. Then, E_1 produces an effective barrier $\phi_{\text{eff}} = E_1 - E_F$ even if ϕ collapses,[20] so that the transport takes place via tunneling (between the disturbed states of the tip and the sample surface).

2.1.3 Point contact regime

As the tip approaches the sample further ($s \leq 2$ Å), a quantum point contact is initiated by chemical bonds formed between the tip and sample atoms. The effective barrier ϕ_{eff} diminishes, and some electrons can propagate freely through the orifice between the tip and the sample surface leading to ballistic transport.

Gimzewski and Möller[2] achieved the formation of a point contact by a clean
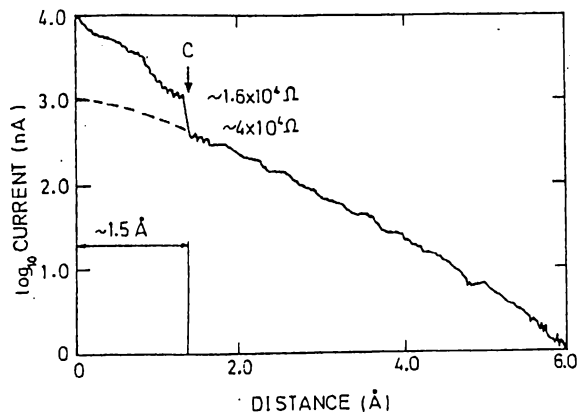
Figure 2.1: Tunneling current ($\log I$) versus distance s for a clean Ir tip and polycrystalline Ag surface at constant bias voltage 20 mV. [Refs. 2 and 24].

metallic (Ir) tip pressing the Ag surface. By measuring $\log I$ versus s curve they found important deviation form simple exponential behavior as illustrated in Fig. 2.1. Deviations are seen more clearly in Fig. 2.2 in which selected data are shown.[21] At small excursions ($\Delta z \leq 3.5$ Å) the separation s between the tip and the sample is relatively large, and the curve is typical for tunneling. The apparent barrier height ϕ_{eff} is as high as 3.5–5 eV in STM mode. As the tip approaches towards the surface, the barrier height is reduced resulting in a plateau in $\log I$ versus s curve corresponding to a saturation resistance R_s. Lang[21] calculated the resistance plateau using the adatom-on-jellium model for a Na atom tip, and found $R_s = AR_c$ where $R_c = h/2e^2 \approx 12900$ Ω is the constriction resistance[22] associated with a one dimensional conduction channel which connects two reservoirs, and A is a constant (higher than unity[21]) depending on the kind of the tip atom.
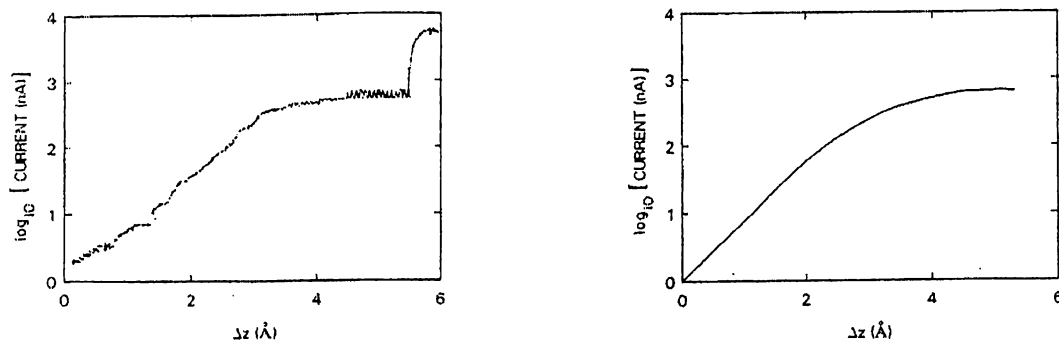
Figure 2.2: Tunneling current ($\log I$) versus excursion Δz measured from the starting point where the resistance is 20 MΩ (at constant bias voltage 20 mV). Left panel: Experimental result for a clean Ir tip and polycrystalline Ag surface. Right panel: Theoretical result for a Na atom tip. [Refs. 2 and 21].

On further decreasing the separation s, a discontinuous jump occurs in current. Consequent abrupt change in resistance (approximate values given in Fig. 2.1) indicates the onset of quantum point contact. Gimzewski and Möller estimated an initial contact radius, r_c, of 1.5 Å according to the Sharvin formula assuming $r_c \ll l_e$, and they concluded that initially the contact must be of

atomic dimensions. A hysteresis pattern suggesting adhesion occurs between tip and sample was also observed in the experiments with large excursions ($\Delta z > 5$ Å), whereas the variation of $\log I$ is reversible for $\Delta z < 5$ Å. In conjunction with these results, Sutton and Pethica[23] demonstrated strong adhesion between clean surfaces (involving inelastic flow) which makes the tip and the sample jump to contact with very small separations (~ 1.5 Å in Fig. 2.1). In this way, discontinuous jump in current is attributed to mechanical instability caused by atomic motion under the influence of adhesive forces. Moreover, in a tight-binding study Ferrer *et. al.*[24] argued that the tunneling resistance should saturate at a minimum value of $R_s = R_c$ if no instability would occur at the onset of point contact.

2.2   STM Studies of Graphite

The two forms (hexagonal and rhombohedral) of graphite cannot be isolated and single crystals are difficult to obtain and their size is generally small. For these reasons, polycrystalline pyrographite is usually studied in scanning tunneling microscopy (STM). The most widely used form is highly oriented pyrolitic graphite (HOPG) whose misorientation angle is less than 2 degree.[15] The scan size in a typical STM study is smaller than the grain size ($3 - 10 \ \mu m$) of HOPG,[15] hence it provides atomically flat surfaces of sufficiently large area. Together with that, the easy preparation of HOPG sample (simply by cleaving), and the inertness of the graphite surface towards chemical reactions have made graphite the standard test and calibration sample.

As explained in Sec. 3.1, the carbon atoms in an ideal graphite (0001) surface form honeycomb structure. Three alternating atoms of each hexagon (specified as A sites of the lattice) lie in a different environment than the other three atoms (B sites). While A sites face A sites directly below in the adjacent layer, B sites face the center of the hexagons (H sites). The atomic flatness of large terraces of cleaved graphite was confirmed by STM images in early experiments performed in ultra-high vacuum (UHV) and in air. However, (0001) surface was seen as

a triangular lattice, rather than a honeycomb lattice. The spacing between the topographic maxima was found equal to the second-nearest-neighbor distance of graphite. Electronic structure calculations,[25,33] later, showed that B sites exhibit a higher LDOS at Fermi level than A sites; H sites exhibit the lowest. Thus, only B site atoms were expected to be seen as protrusions; A sites should appear as saddle points, and H sites should result depressions. This phenomena is denoted as the site asymmetry. It was found nearly independent of polarity within bias voltage range $[-0.2, 0.2]$ V, and this independence is attributed to atomic force interactions. On the other hand, site-selective imaging[26] of A and B sites can be achieved by reversing the bias polarity when the bias voltage is larger than a threshold value $(0.5$ $V)$.

Bias dependent STM studies yield also important information on the sample electronic structure. Experimentally, the decrease of the corrugation amplitude was observed with increasing bias voltage as, indeed, predicted earlier by theoretical analysis.[27] This decrease was noticed only at high voltages if the tip-sample interaction dominates.[28]

The site asymmetry would not be expected to exist for graphene, *i.e.* a monolayer extracted from graphite. However, triangular arrangement of maxima are seen in STM images of graphene on a Pt(111) surface.[17] The Fermi surface of graphene reduces to a point at the edge of the Brillouin zone. Consequence of that is imaging a single state. The nodes of the wave function of this individual state do not depend on the atomic position in the unit cell and lead to large corrugations with the periodicity of the unit cell.[29] In bulk graphite, the Fermi surface is very narrow, but finite because of the weak interlayer interaction, and lifts the nodes of the wave function. Nevertheless, the image is dominated by the same individual state.[33]

In the STM studies of graphite, giant corrugations (up to 8 Å or even more) are often observed in the constant current mode of operation. The corrugation of 0.8Å was calculated for contours of constant LDOS at Fermi level, which flatten out to 0.2 Å (also determined by helium diffraction data) for the contours of total charge density. While imaging a single state, the nodal structure of the wave

function enhances the corrugation amplitude up to 1 Å.[29] Beyond this value, giant corrugations are attributed to local elastic deformations[28] of the surface that are induced by atomic force between the tip and the sample. Such deformations enhance the corrugation due to the electronic density of states. This explanation is also confirmed by experiment: The corrugation amplitude was found smaller than 0.1 Å under the condition of free tip-sample mechanical interactions.[26]
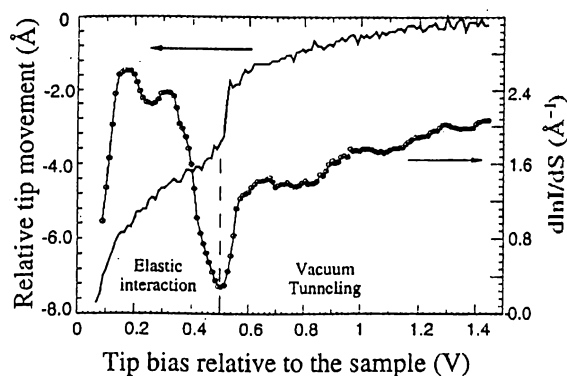
Figure 2.3: The measurement of the tip movement and $d\ln I/ds$, as a function of the tip bias at a constant tunneling current of 1 nA. [Ref. 26].

Transition to the elastic deformation regime is clarified in Fig. 2.3 by the variation of the decay rate κ. At about 0.5 V, the barrier height ϕ (which is related to $2\kappa = d\ln I/ds$) collapses. Nevertheless, it remains finite even at that value of the bias voltage. Below this transition voltage, $d\ln I/ds$ has no relevance to ϕ because of elastic deformations which are also indicated by nonlinear variations of the tip movement.

Chapter 3

ATOMISTIC SIMULATIONS

3.1 Atomic Structure of Graphite

Graphite has a hexagonal lattice structure with lattice constants a and c as defined in Fig. 3.1. It posses a layered structure with honeycomb arrangements of carbon atoms on (basal) planes. The layers are weakly bonded to one another, but also well separated. Experimental values of the nearest neighbor distance $(a/\sqrt{3})$ and the interlayer spacing $(c/2)$ are respectively 1.42 Å and 3.337 Å at zero temperature,[30] and 1.418 Å and 3.348 Å at room temperature.[31] Since c to a ratio is much greater than the ideal closed-packed value, graphite is far from being hexagonal closed-packed.

Graphite is the most stable allotrope of carbon, except that diamond is more stable at very high pressures. The interatomic distance (1.418 Å) in graphitic plane is shorter than that of diamond (1.54 Å) and reflects the thermodynamical stability. The diamond value is close to the carbon-carbon single bond length (1.55 Å), whereas that of graphite is stronger than single bond, but yet it is weaker than double bond (which corresponds to 1.33 Å bond length[14]). In this respect, graphite is similar to benzene molecule. Benzene has 1.39 Å bond length,[14] and experimental fact[32] is that all bond lengths in benzene are equal and lie between that of single and double carbon bonds.

Graphite can be in different forms according to the stacking of its basal

planes. The most common form is the hexagonal (Bernal) graphite with *ABAB* stacking of layers. In rhombohedral graphite, layer stacking is *ABCABC*; the *AAA* sequence occurs in first stage intercalates, *e.g.* alkali metal intercalated graphite. Intercalation describes the insertion of guest agents between graphite layers with metallic-type bonds. In pseudopotential calculations,[34,33] total energy differences were found to be smaller than 0.005 eV per atom among these three forms, showing also the weakness of interlayer interaction. In the weak interlayer interaction the Van der Waals bonding between widely separated graphitic planes has a significant contribution. On the other hand, planar bonds are strong covalent bonds with sp^2 hybridization of carbon electrons. With this anisotropy in bonding, graphite is highly ordered within layers but stacking sequence may

$$\mathbf{R}_1 = a\,\mathbf{x}$$

$$\mathbf{R}_2 = a\left(-\frac{1}{2}\mathbf{x} + \frac{\sqrt{3}}{2}\mathbf{y}\right)$$

$$\mathbf{R}_3 = c\,\mathbf{z}$$

$$\beta : \quad \tau_1 = 0$$

$$\alpha : \quad \tau_2 = a\left(\frac{1}{2}\mathbf{x} + \frac{1}{2\sqrt{3}}\mathbf{y}\right)$$

$$\alpha' : \quad \tau_3 = a\left(\frac{1}{2}\mathbf{x} + \frac{1}{2\sqrt{3}}\mathbf{y}\right) + \frac{1}{2}c\,\mathbf{z}$$

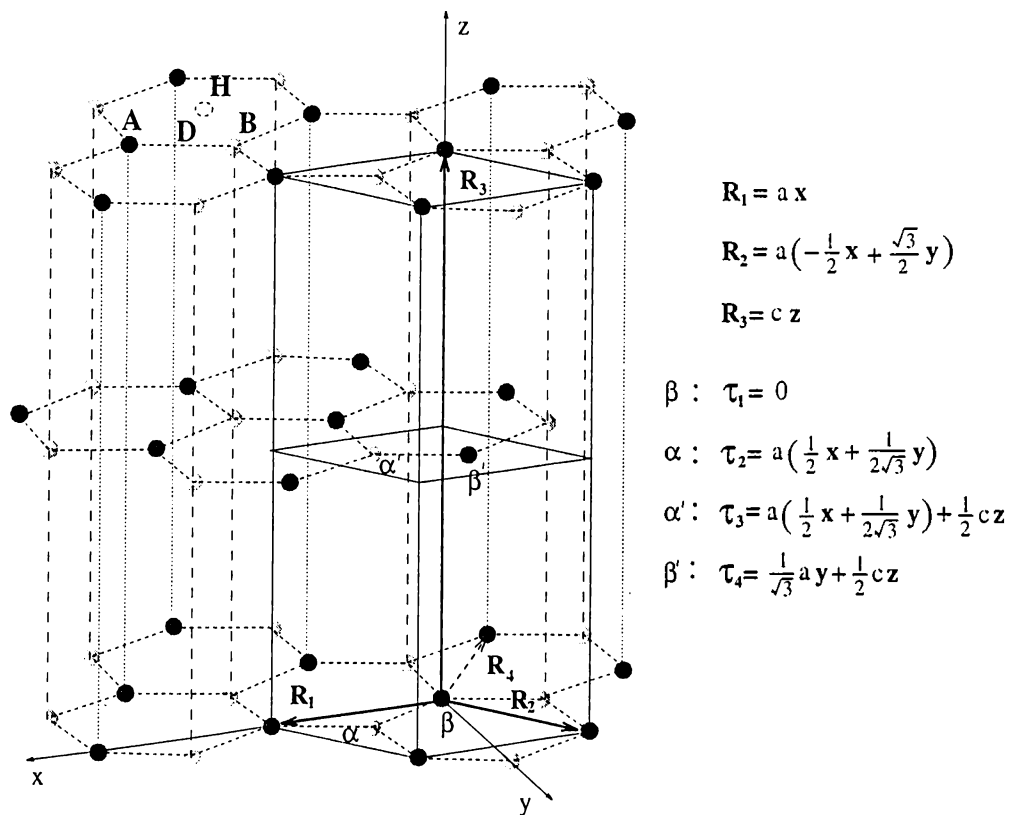$$\beta' : \quad \tau_4 = \frac{1}{\sqrt{3}}a\,\mathbf{y} + \frac{1}{2}c\,\mathbf{z}$$

Figure 3.1: Graphite in Bernal Structure

be erratic, or can be made erratic *e.g.* by pyrolizing. This general form is called pyrographite, or pyrolytic graphite.[14]

The Bernal structure has two inequivalent atoms (α', β' in the planar unitcell drawn in Fig. 3.1) per layer, and layers are staggered so that each α atom has atoms α' directly above and below in adjacent layers whereas β sees hollow center of corresponding hexagon. β' is on the center of the neighboring hexagon. The structure can also be described as combining two hexagonal lattices of α and β atoms. The unitcell is then defined by the primitive vectors $\mathbf{R}_1$, $\mathbf{R}_2$, $\mathbf{R}_3$ of these lattices as shown in Fig. 3.1. $\mathbf{R}_4$ is added to represent the surfaces in a more appropriate way. In hexagonal systems, the surfaces are labeled by four indices ($ijkl$) corresponding to the vectors $\mathbf{R}_1$, $\mathbf{R}_2$, $\mathbf{R}_4$, $\mathbf{R}_3$. The index along $\mathbf{R}_4$ is always related to two of others: $k = -(i+j)$. In such a labeling system, the top layer, for instance, is represented by (0001). There are four atoms in the unitcell with the position vectors τ_1, τ_2, τ_3, τ_4. In this work, the positions of α and β atoms are labeled as A and B sites respectively. The center of hexagon is H site; the mid-point between α and β atoms is labeled as the bridge D site.

3.2 Interatomic Carbon Potential

The interatomic potential V used in this work was developed by Nordlund *et al.*[35] (to its final form) by combining three distinct potentials:

$$V(r_{ij}) = [V_T(r_{ij}) + V_G(r_{ij})]F(r_{ij}) + V_R(r_{ij})[1 - F(r_{ij})], \qquad (3.1)$$

where r_{ij} is the distance between ith and jth atom. The total energy of the atomic system (in a given configuration) E is then expressed as a summation over all atom pairs:

$$E = \frac{1}{2} \sum_{i \neq j} \sum V(r_{ij}), \qquad (3.2)$$

in terms of the interatomic interaction energy $V(r_{ij})$. This description seems to be similar to that of pair potentials, however, there is an important difference due to the implicit many-body interactions in V_T and V_G. Nevertheless, it also

differs from cluster potentials in that there is no summation over higher-order atom multitudes.

Despite the fact that the potential describes several carbon polytypes reasonably; the combination of three potentials are mainly required for graphite. The main contribution, the Tersoff potential[37] V_T, gives a good description of covalent bonding, and describes diamond and graphene fairly good. But, unfortunately, its range is so short that the weak interaction between graphite layers is not included. For this reason, Nordlund *et. al.*[35] introduced a long-range potential V_G to include bonding between graphite layers. Besides, a repulsive *ab initio* potential V_R is included in order to treat the strong repulsion between the atoms when the interatomic distance is very small. This repulsive potential prevents the structure from collapsing.

Tersoff[36] had gone beyond the conventional two- and three-body potentials in transferability and accuracy by introducing a new family in view of the quantum-mechanical arguments. Main observations were the universal binding-energy curve of Rose *et al.*[39,40] and its exponential parameterization given by Abell.[41] Rose *et al.*[39,40] have shown that the binding energy versus atomic separation curve can approximately be scaled into a single universal relation for metallic adhesion and the cohesion of bulk metals. This universal form predicts the curve relative to the equilibrium. Abell[41] parameterized the binding energy (within local orbital chemical pseudopotential theory) as Morse-like pair potentials to guarantee the universality. Moreover, he made an interpretation of the Pauling's bond order,[42] *i.e.* the strength of the bonding with respect to the bond length, to include the topologic effects relative to a reference system. These ideas are incorporated in the empirical potential by Tersoff,[38] introducing exponential pair potentials, and realizing the bond order as depending on the local atomic environment. Hence, the potential was designed in the following functional form:

$$V_T(r_{ij}) = f_C(r_{ij})[f_R(r_{ij}) + b_{ij}f_A(r_{ij})], \tag{3.3}$$

with a repulsive pair potential f_R expressing the orthogonalization energy of

overlapping atomic wave functions:

$$f_R(r_{ij}) = A \, e^{-\lambda r_{ij}}, \tag{3.4}$$

and an attractive pair potential f_A associated with bonding:

$$f_A(r_{ij}) = -B \, e^{-\mu r_{ij}}, \tag{3.5}$$

and a smooth cutoff function f_C to shorten the range of the potential for fast computations:

$$f_C(r_{ij}) = \begin{cases} 1, & r_{ij} < R \\ \frac{1}{2} + \frac{1}{2} \cos(\pi \frac{r_{ij}-R}{D-R}), & R < r_{ij} < D \\ 0, & r_{ij} > D \end{cases} \tag{3.6}$$

In Eqns. (3.4) and (3.5), parameters A and B restrict the strength of repulsion and attraction respectively, and λ^{-1} and μ^{-1} determines the range of the corresponding potentials. R in Eqn. (3.6) is the actual range of the complete potential; from R to D the potential goes to zero. Beyond D, there is no interaction in any pairs.

In Eqn. (3.3), b_{ij} is a measure of the bond order. The determination of a satisfactory form of this term is the key point of Tersoff potential. As discussed by Abell[41] and Tersoff,[38] the bond order is a monotonically decreasing function of atomic coordination number Z, *i.e.* the number of neighbors close enough to form bonds. Moreover, as also observed in *ab initio* calculations,[43] b_{ij} must grow more rapidly than $Z^{-1/2}$ with decreasing coordination, and saturate at low coordination to give an energy minimum at an intermediate coordination. To satisfy this behavior, Tersoff[38] assumed that

$$b_{ij} = (1 + \beta^n \zeta_{ij}^n)^{-1/2n}, \tag{3.7}$$

where the effective coordination term ζ_{ij} counts the other bonds of the ith atom beside the ij bond:

$$\zeta_{ij} = \sum_{k \neq i,j} f_C(r_{ik}) \, g(\theta_{ijk}) \, \epsilon(r_{ij}, r_{ik}) \tag{3.8}$$

The cutoff function f_C takes kth atom (as a bonding neighbor) into account if it is sufficiently close to ith atom. The existence of such a bonding neighbor decreases b_{ij}, and therefore interaction energy of the ij pair is reduced. As a result the ij bond is weakened. In Eqn. (3.7), the parameters β and n are introduced to yield a proper generalization of the coordination number. The function g treats the bond-angle forces within the effective coordination term:

$$g(\theta_{ijk}) = 1 + \frac{b^2}{d^2} - \frac{b^2}{d^2 + (u - \cos\theta_{ijk})^2}, \qquad (3.9)$$

where θ_{ijk} is the angle between two bonds, ij and ik. The parameter u corresponds the cosine of the energetically optimal angle, d determines how sharp the dependence on angle is, and b measures the strength of the angular effect. With these, g is constrained to the correct angular coordination within local environment of any atom. The other function ϵ gives yet another cutoff for bonding of neighbors,

$$\epsilon(r_{ij}, r_{ik}) = e^{\eta^3 (r_{ij} - r_{ik})^3}, \qquad (3.10)$$

where η^{-1} determines the range of bonding. If the parameter R allows only first-neighbor interaction within a model description, η is effectless unless it equals to μ. In any case, η can be set to equal to μ.

The bond order b_{ij} depends upon the local coordination of the ith atom with its neighbors, making the potential more transferable. Transferability, in such a classical model, means the ability of correct description of the interaction between atoms under different local environments. In this model, it is clear that the interaction energy of a pair differs as its surrounding changes. Furthermore, the contributions of a pair of atoms are not equal in a given configuration due to the asymmetry in bond order, *i.e.* $b_{ij} \neq b_{ji}$, and hence $V(r_{ij}) \neq V(r_{ji})$.

In the present implementation, the first and second nearest neighbors are in the range of V_T, so none are accounted for different layers. In contrast, V_G takes the main contribution from neighboring atoms on adjacent layers, and negligible amount from the ones within the same layer (by the effect of ϕ_3 defined below). The two potentials are then of different ranges, and summing up the two does not destroy the description of the relevant potential in its own range. In this way,

an independent extension of the potential is achieved to give nonzero interlayer forces that are completely absent in Tersoff potential. V_G is mainly a Morse potential V_M fitted to the experimental force curve[35]. However, as mentioned before, a many-body term ϕ_3 is also introduced for interplanar bonding, which simultaneously reduces V_M within a monolayer. Therefore,

$$V_G(r_{ij}) = \begin{cases} 0, & r_{ij} < r_{M,0} \\ \phi_3(G_{ij})V_M(r_{ij}), & r_{M,0} < r_{ij} < r_{M,1} \\ 0, & r_{ij} > r_{M,1} \end{cases} \qquad (3.11)$$

with

$$V_M(r_{ij}) = V_{c_0} - (e^{-l_4(r_{ij}-c_0)} - 1)^2. \qquad (3.12)$$

The reason for the low-end cutoff $r_{M,0}$ is explained above, and the high-end cutoff $r_{M,1}$ is introduced for efficient molecular dynamics simulations,[35] *i.e.* for computational purposes. V_{c_0} is a parameter to adjust the minimum of the interlayer interaction energy, c_0 is formally the equilibrium interlayer spacing, and l_4 determines the range of the interlayer interaction. In Eqn. (3.11), the many-body term is G_{ij} with the following definitions:

$$\phi_3(G_{ij}) = -\frac{l_0}{1 + (\frac{G_{ij}-3}{l_3})^2}, \qquad (3.13)$$

$$G_{ij} = \sum_{k \neq i,j} \phi_1(\theta_{ijk})\phi_2(r_{ik}). \qquad (3.14)$$

Without being affected very much by the value of G_{ij}, the parameter l_0 reduces the Morse potential by a few order of magnitude. The effect of ϕ_3 is to reduce high-energy contributions of three first-nearest neighbors. $-V_{c_0}l_0$ is the interaction energy between layers (through α atoms) without three-body modulations which is through the following functions:

$$\phi_2(r_{ik}) = \frac{1}{1 + (\frac{r_{ik}-r_0}{l_2})^4}, \qquad (3.15)$$

$$\phi_1(\theta_{ijk}) = \frac{1}{1 + (\frac{\cos\theta_{ijk}}{l_1})^4}. \qquad (3.16)$$

ϕ_2 makes the first-neighbors effective in bonding of planes (as long as parameter r_0 chooses first neighbors within a range determined by l_2) whereas ϕ_1 prefers the triples with an angle close to the right angle (provided by the value of parameter l_1). Therefore, there is a trade-off in between to optimize the effect of the surroundings of atom pairs. Consequently, the planar bonding is basically between the α and α' atoms of successive layers of graphite. Because the coordination number of graphene, *i.e.* 3, is subtracted from G_{ij} to tolerance to l_3, ϕ_3 prevents high energy contributions of three nearest-neighbors of an atom when it is binding to adjacent layers.

The third potential V_R in Eqn.3.1 is the repulsion energy of carbon-carbon dimer. It is of the form of numerical data[44] obtained by doing spline interpolation to the results of dense density functional calculations within the local density approximation.[35] V_R is smoothly fitted to the Tersoff potential as expressed in Eqn. (3.1) by using the following Fermi function:

$$F(r_{ij}) = \frac{1}{1 + e^{-b_f(r_{ij} - r_f)}}. \qquad (3.17)$$

With this fitting the interaction between two atoms which are closer (further) than r_f is effectively determined by V_R (V_T). b_f gives the range of transition from V_R to V_T.

The parameters of the potential were determined by Tersoff[37] and Nordlund *et al.*[35] V_T is fitted to the cohesive energies of carbon polytypes, along with lattice constants and bulk modulus of diamond. The results of *ab initio* calculations[43] were used when measurements became unavailable. Tersoff determined the parameters R and D somewhat arbitrarily, and set η equal to zero for simplicity. The parameters in V_G and F are determined by experimental data[45,46] and by fitting of the interplanar energy versus lattice parameter c curve to the experimental one,[46] and by another energy fitting to the diamond-to-graphite transition curve.[47] Nordlund *et al.* optimized the parameter D, and set η equal to μ. The final parameters are as follows: $R = 1.8$ Å, $D = 2.46$ Å, $A = 1.3936 \times 10^3$ eV, $\lambda = 3.4879$ Å^{-1}, $B = 3.467 \times 10^2$ eV, $\mu = 2.2119$ Å^{-1}, $\beta = 1.5724 \times 10^{-7}$, $n = 7.2751 \times 10^{-1}$, $\eta = 2.2119$ Å^{-1}, $b = 3.8049 \times 10^4$,
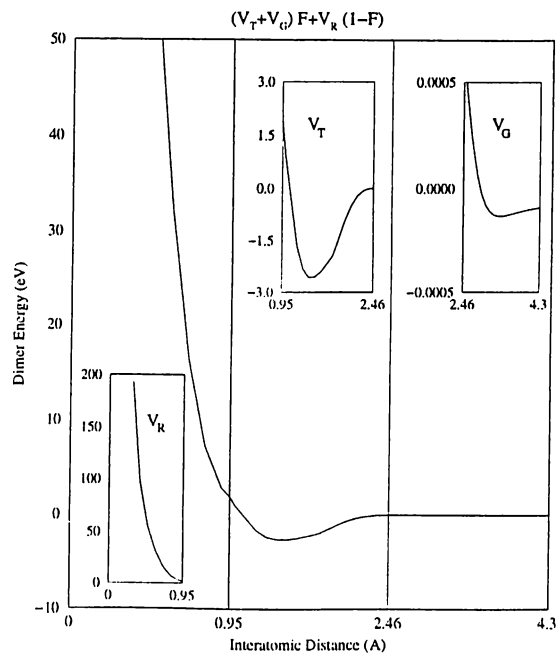
Figure 3.2: The energy of the carbon dimer. The ranges of V_R, V_T and V_G become clear in the insets. The extension of the range of the Morse potential results a very weak barrier as shown.

$d = 4.3484$, $u = -5.7058 \times 10^{-1}$, $c_0 = 3.348$ Å, $l_0 = 0.0456$ eV, $l_3 = 0.15$, $r_0 = 1.46$ Å, $l_2 = 0.21$ Å, $l_1 = 0.07$.

In addition to what is described above, a minor modification of the potential was made in the present study. Owing to the transition data in its construction, the potential is able to choose the right local (tetrahedral) environment rather than the graphitic coordination under the influence of high pressure. However, there is a gap in the case of uniaxial compression between interlayer spacing values 2.46 Å and 2.87 Å as it is well understood from the given parameters that the potential becomes identically zero in this range (without destroying the quality of predictions for near-equilibrium properties of graphite). A linear interpolation of V_T and V_G is made from 1.8 Å to 2.87 Å keeping the parameters unchanged. The range of V_G is extended towards that of V_T in this way; the effect of this modification is seen in Fig. 3.2 for carbon-carbon dimer by adding a very weak
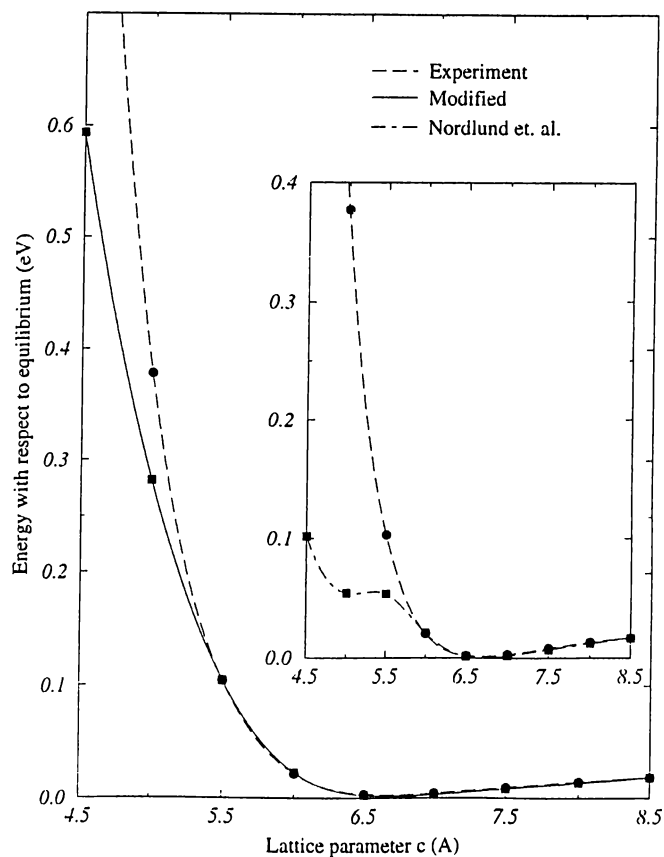
Figure 3.3: Total energy versus lattice parameter c. The zero of the energy is set to the equilibrium value at $c = 6.696$ Å.

barrier to the potential. As shown in Fig. 3.3, the combination of V_T and V_G results in a flat region near the vicinity of the equilibrium, and the slope gained by the Tersoff potential remains too small in comparison with the experimental curve. The interpolation extends the range in which the interlayer energy curve lies close to the experimental one. The transferability of the potential is not destroyed, and is slightly improved for high-coordinated structures as seen in Fig. 3.4. In addition, the energy versus interatomic distance curves for all carbon polytypes mentioned in Fig.3.4 do not differ significantly from those of the form that was used by Nordlund *et al.*[35] near the equilibrium. Finally, the linear interpolation is assumed to be crude in calculating forces, but no instabilities
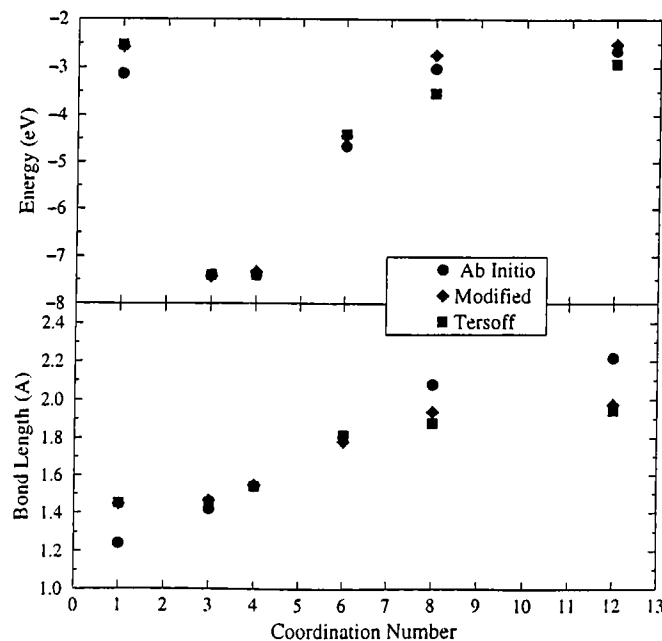
Figure 3.4: The transferability of the interatomic carbon potential. The values on horizontal axis represents dimer(1), graphite(3), diamond(4), simple cubic(6), body-centered cubic(8), and face-centered cubic(12) structures, in order.

(arising from jumps in force in the range of interpolation) are identified in molecular dynamics simulations. Hence, even though the interpolation made may be regarded as an artificial procedure, the resulting form of the potential is reliable for simulation purposes as much as the previous forms.

Any binding phenomenon corresponds to a (local) minimum in Born-Oppenheimer (BO) potential energy surface, *i.e.* the configuration energy with respect to atomic degrees of freedom. The potential given above is capable of describing BO surface since the bond order b_{ij} follows the variations of BO surface with respect to atomic positions: The attraction of atom pairs is modulated by b_{ij}; the values of b_{ij}'s depend on the position of the atomic configuration relative to the extrema of the BO surface. This feature makes the potential favorable for molecular dynamics simulations. As an example, binding of a single carbon atom to (multilayer) graphite is illustrated in Fig. 3.5. When the atom is about
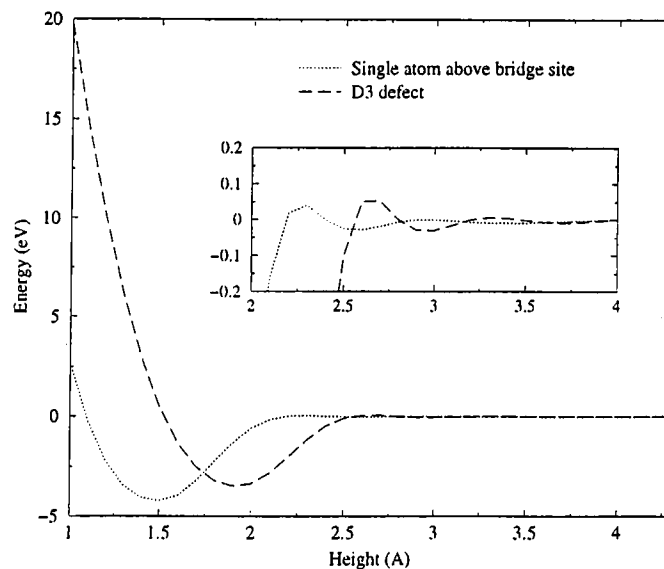
Figure 3.5: Binding of a single carbon atom to the graphite lattice.

1.5 Å above D site, binding occurs with an energy of -4.21 eV. If a graphitic plane was present in place of the single atom, there would be strong repulsion as deduced from Fig. 3.3. Thanks to the presence of b_{ij} term, the bond order tends to vanish in the case of a graphitic plane whereas it is nearly unity for the single atom. The other curve in Fig. 3.5 is an additional example, and is drawn to determine the binding energy of a $D3$ defect, *i.e.* a surface defect formed by an atom above D site which lifts two neighboring atoms (α and β) on the top layer. These three atoms form a vertical ring whose shape is nearly equilateral triangle. The topmost atom and the neighboring α and β atoms are about 2 Å and 0.4 Å higher than undisturbed lattice, respectively. The distance between α and β atoms is approximately 7% longer than the equilibrium value. Nordlund *et al.*[35] verified that the $D3$ defect structure is stable, and suggested that it may be source of hillocks higher than 2 Å observed experimentally. Their *ab initio* calculation gave a binding energy of -3.3 eV. The interatomic potential yields -3.33 eV at 2 Å, however the minimum of energy (-3.46 eV) is at 1.9 Å.

3.3 Molecular Dynamics Simulations

The formation of an atomic-size contact on the graphite (0001) surface is simulated by using the classical molecular dynamics (MD) method with the empirical potential described in the previous section. In this section, a brief summary of classical MD method is presented, and the results of the simulations are discussed. In the classical MD method, the atomic interactions are modeled by an empirical potential, and Newtonian equations of motion are solved for each atom in the system by a finite difference method which is 7-Value Gear predictor-corrector in this work. The algorithm of the computations is simply as follows:

1. Predict the positions and derivatives at time $t + \tau$ by making a Taylor expansion about time t:

$$
\begin{aligned}
\mathbf{r}^p(t + \tau) &= \mathbf{r}(t) + \tau\mathbf{v}(t) + \frac{1}{2}\tau^2\mathbf{a}(t) + \cdots, \\
\mathbf{v}^p(t + \tau) &= \mathbf{v}(t) + \tau\mathbf{a}(t) + \cdots, \quad \text{up to sixth order}
\end{aligned}
$$

2. Evaluate forces from the gradient of the interatomic potential energy:

$$
\mathbf{F}_i = -\nabla_{\mathbf{r}_i} E
$$

3. Correct predicted quantities using the Gear corrector coefficients $c_0, c_1, \ldots$

$$
\begin{aligned}
\mathbf{r}^c(t) &= \mathbf{r}^p(t) + c_0[\mathbf{a}^c - \mathbf{a}^p], \\
\mathbf{v}^c(t) &= \mathbf{v}^p(t) + c_1[\mathbf{a}^c - \mathbf{a}^p], \quad \text{up to sixth order}
\end{aligned}
$$

4. Calculate any variables of interest

The system investigated is a tip-sample system which is represented by two models of different size. The sample is a graphite slab comprising 6 (or 8) layers, *i.e.* (0001) planes. Each layer contains 308 (or 448) atoms, making total number of sample atoms 2016 (or 3584). The hard and sharp metal tip (such as W) is represented by a robust diamond tip; it comprises 13 (111) diamond planes, and

contains 167 atoms. The apex of the tip has a single atom, and the higher layers contains $3, 3, 6, 6, 10, 10, 15, 15, 21, 21, 28, 28$ atoms, in order. Periodic boundary conditions are imposed to the slab only in the lateral directions (x and y), and the tip is not periodic at all. The system is divided into static and dynamic regions in an artificial way; all atoms belonging to the tip and to the lowest two layers of the sample are kept fixed in the integration procedure. The remaining atoms are treated dynamically. The temperature is rescaled to 2 K at every two steps to avoid possible divergences in the kinetic energy of moving atoms. The time step was $\tau = 1 \times 10^{-16}$ in accordance with high-order Gear algorithm.[48]

Initially, the tip is at $s = 2.5$ Å above the sample, and then it is pushed down towards the sample in the course of the simulation. The strategy of pushing the tip towards the sample is as follows: The sample is first equilibrated in 500
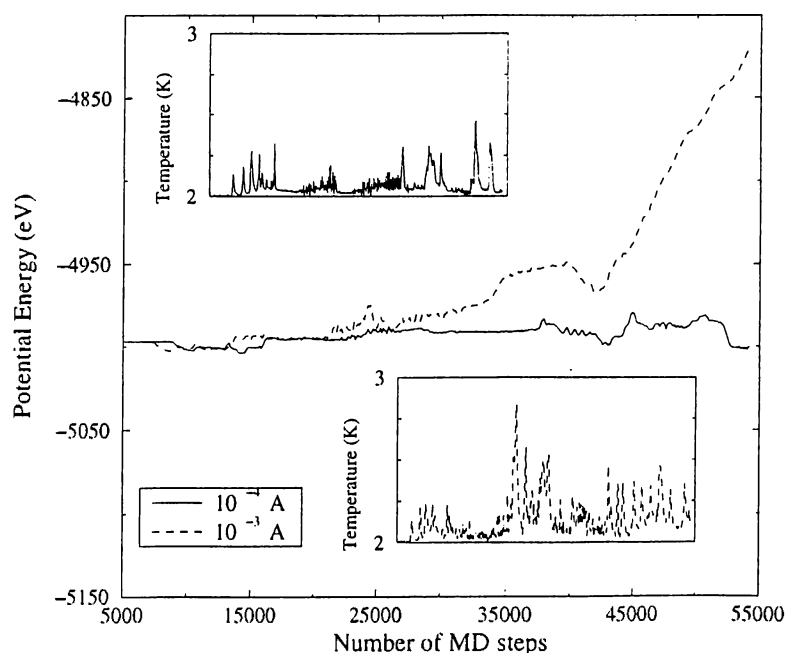

Figure 3.6: Variation of the potential energy and convergence of the temperature during test simulations. The tip and sample are in highly repulsive interaction. 5000 relaxation steps were needed to equilibrate the system fully before the push of the tip starts.

relaxation steps before the start of pushing. Since the interaction is very weak between the sample and the tip, that amount of time is found to be sufficient. The equilibration is terminated when the fluctuations in the total energy settled down. Then the tip is pushed at a rate of 1×10^{-4} Å per time step for 500 steps, and then the system is relaxed during the next 500 steps. The velocity of the tip (100 m/s) is small enough to allow the system reequilibrate between successive instabilities if any occur. At the end of each 500 relaxation steps total energy fluctuations settle down, and the temperature converges to 2 K.

Some test calculations are performed to find a reliable and fast strategy of pushing. The rate of pushing should be large enough to avoid the long simulation times. On the other hand, it should be sufficiently small in order to fully equilibrate the system. Simulations with two values of the pushing rate (1×10^{-3} Å and 1×10^{-4} Å) are compared in Fig. 3.6. The smaller value seems to be more appropriate for stable simulations.

3.3.1   Results and Discussion

The tip is located at various positions (A, B and H sites) in the xy-plane, and it is pushed towards the surface at constant x and y. Relatively large relaxations occur initially in the course of pushing the tip. Near the contact the tip compresses the slab, and eventually punctures the topmost layer. These variations are more clearly seen in Fig. 3.7, where the solid lines represent the undisturbed layers; the dashed lines show the average changes in layer heights; the dotted lines show the variations of the positions of the atoms within close proximity of the tip apex of the first and second layers. The heavy line represents the tip position. In the lower panel, the variation of the force on sharp tip is shown. Figs. 3.8 and 3.9 include the same information for H and A sites, respectively.

At the beginning, the tip is 2.5 Å above the surface where there is attractive tip-sample forces in all three cases. When it is pushed down by 1 Å above B site repulsive forces increase. The slab is then compressed by dominant repulsive forces until the downwards displacement of the tip reaches to 4 Å. At this value
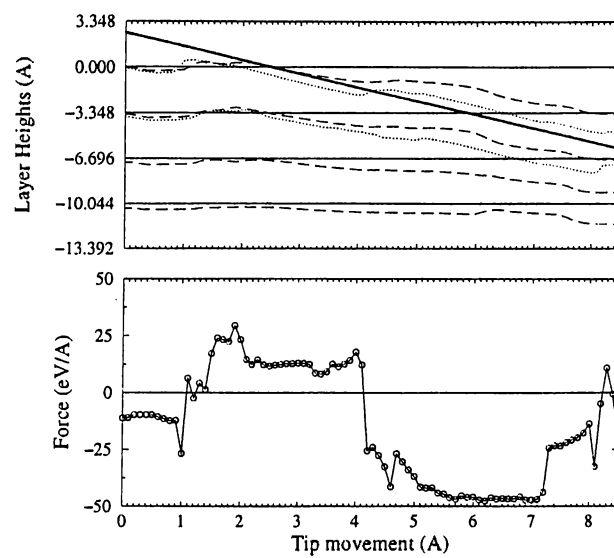
Figure 3.7: The variation of the layer heights and the force with the movement of the tip above B site.
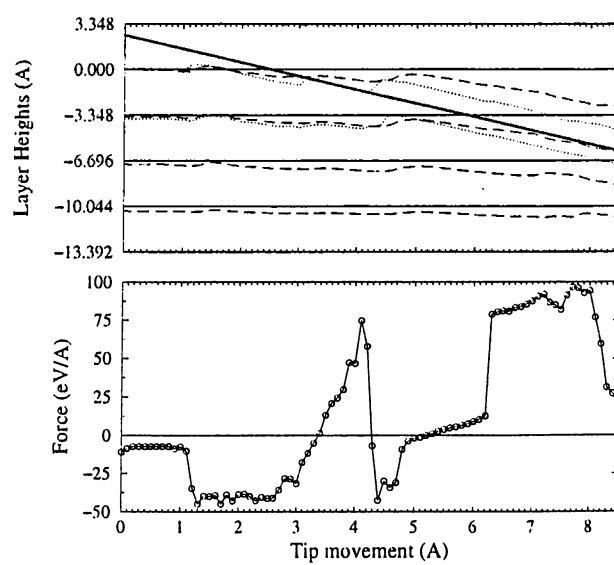

Figure 3.8: The variation of the layer heights and the force with the movement of the tip above H site.
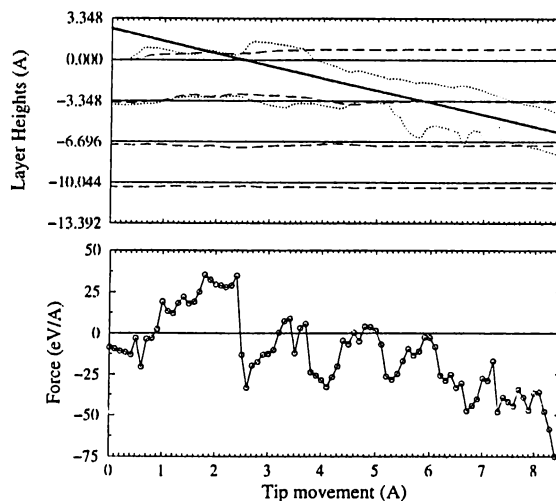
Figure 3.9: The variation of the layer heights and the force with the movement of the tip above A site.

sudden transition to attractive interaction is attributed to the puncture of the topmost layer.

It is exciting to observe that the force characteristics for the B (H) site converts into that for the H (B) site in the course of the push. This is what one normally expects from the atomic structure since B and H sites change alternatively in successive graphitic planes, and gives further evidence for successive puncturing of layers.

Fig. 3.9 explains local deformations more clearly. In Figs. 3.10, 3.11, 3.12 and 3.13 some important snap-shots of the simulations are shown for the tip above A site. In this case puncturing is rather fast, and the local environment of the apex follows the tip. The tip enlarges the puncture and eventually breaks the surface into flakes as shown in 3D pictures.

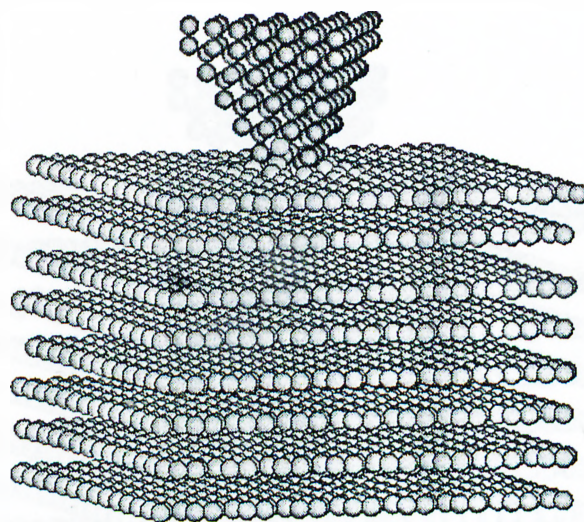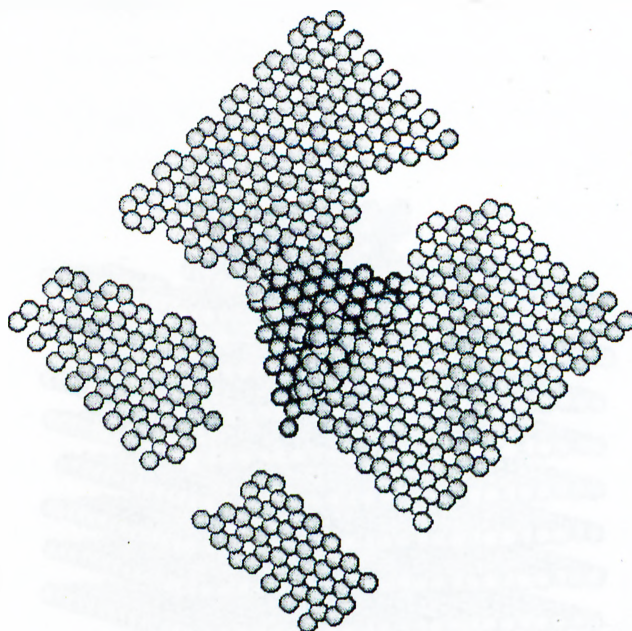Figure 3.10: The puncture of the first layer by the tip above A site.

Figure 3.11: Dislocation-induced crashes in the first layer. Behind is the tip whose apex is between the first and second layers.
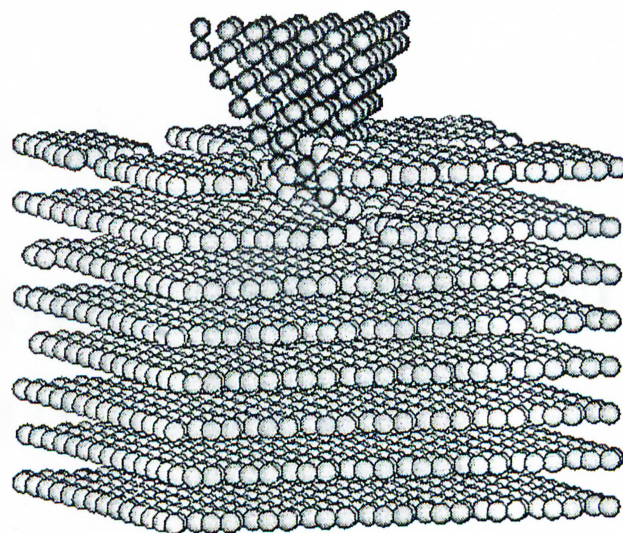
Figure 3.12: The first layer has already been broken into flakes before the tip punctures the second layer.
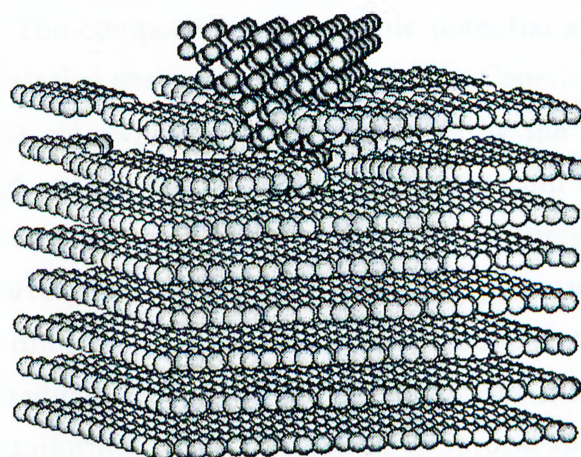
Figure 3.13: Finally, the second layer is also crushed.

Chapter 4

SCF PSEUDOPOTENTIAL CALCULATIONS

4.1 Total Energy Calculations

The self-consistent field (SCF) calculations are performed in momentum space within local density approximation(LDA) to examine the effect of the tip applying a uniaxial strain to the graphite surface. The ionic potential of carbon is replaced by the nonlocal, norm-conserving[49] pseudopotentials taken from the table of Bachelet *et. al.*[50] The components of the ionic potential are shown in Fig. 4.1. The exchange-correlation energy is approximated by Ceperley-Alder (CA) form.[51] A plane wave basis set (whose size is determined by the kinetic energy cutoff $|k + G|^2$) is used within the framework of momentum space formalism[52] of the density functional theory[53] (DFT). The kinetic energy cutoff is taken to be 37 Ry, that corresponds to approximately 900 plane waves for equilibrium structure. The number of plane waves ranges from 550 to 1030 for distorted structures. The irreducible wedge of the Brillouin zone is sampled by 48 points generated from a uniform $6 \times 6 \times 10$ mesh in reciprocal space. The SCF cycles are iterated until the rms deviation of the self-consistent potential is smaller than 1×10^{-7} Ry during each calculation. To test the convergence on the plane wave expansion, some calculations are performed with various kinetic energy
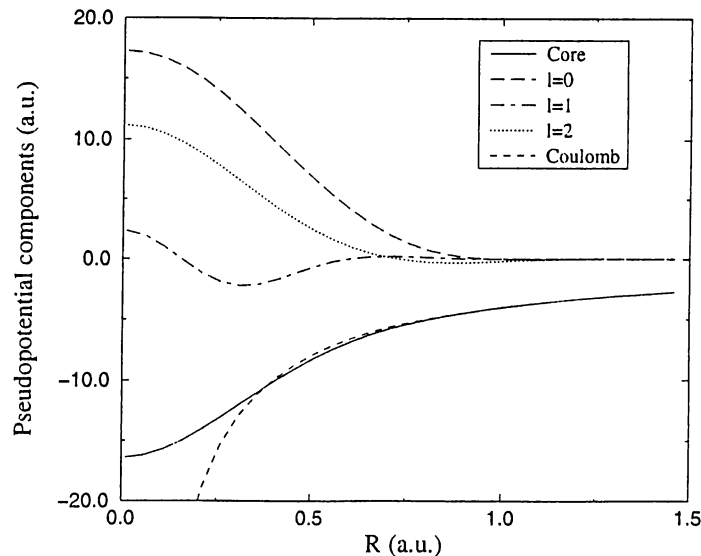
Figure 4.1: The pseudopotential components V_{core}, ΔV_0^{ion}, ΔV_1^{ion}, ΔV_2^{ion} for carbon. The subscript denotes the angular momentum quantum number l. The Coulomb potential is added for comparison. In notation of Ref. 50, V_l^{ion} is decomposed into a long-range Coulomb part V_{core}, and a short range l-dependent pseudopotential part ΔV_l^{ion}.

cutoffs $(33, 37, 39,$ and $45\ Ry)$. The k-point sampling is also tested by the meshes $6 \times 6 \times 6, 6 \times 6 \times 10,$ and $6 \times 6 \times 12$. The change in the total energy is smaller than 0.5% in each case. The accuracy of a standard LDA calculation is expected to be approximately 1%,[54] thus, the calculations in this chapter are considered convenient and sufficiently accurate for the purpose of the present study.

4.2 Band Structure of Graphite

The ground state configuration of carbon is $1s^2\ 2s^2\ 2p^2$. $1s$ electrons are core electrons, and the remaining four are regarded as valance electrons. Bonding in two natural allotropes of carbon *i.e.*, graphite and diamond, is mainly covalent with different hybridization of atomic orbitals. Graphite monolayer, *i.e.* graphene, is made up of strong covalent bonds: three of the valance electrons

$$G_1 = \frac{2\pi}{a}\left(k_x + \frac{1}{\sqrt{3}}k_y\right)$$

$$G_2 = \frac{2\pi}{a}\frac{2}{\sqrt{3}}k_y$$

$$G_3 = \frac{2\pi}{c}k_z$$

Figure 4.2: Brillouin zone of graphite and the irreducible wedge

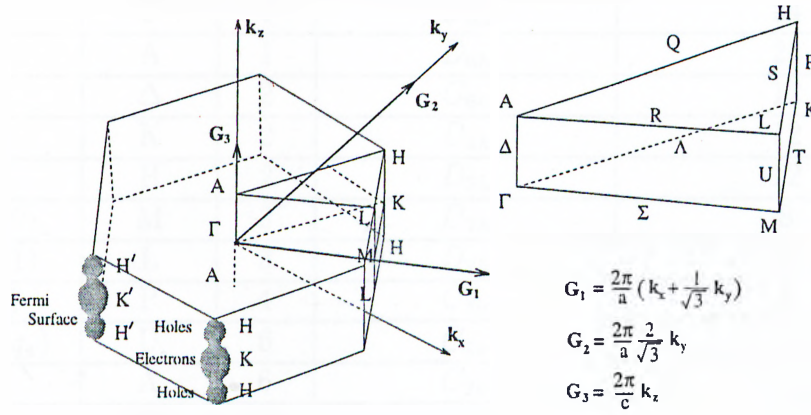(s, p_x, p_y) hybridize to form localized sp^2 bonds, and form σ bonds between two nearest carbon atom in the same plane. The p_z orbitals perpendicular to the layer remain nonhybridized and form delocalized π bonds. The residual interlayer bonding is basically due to the overlap of p_z orbitals and partly due to long-ranged Van der Waals forces, *i.e.* dipole-dipole interaction originated from correlated motion of electrons in different planes,[55] and is very weak in comparison with the intralayer bonding. This binding anisotropy is reflected to the structure of graphite whereas diamond has isotropic structure as a result of sp^3 hybridization.

In the band structure of graphene, sp^2 bonds form three occupied σ bands. Near the Fermi level lie a pair of π bands (one nearly full, the other nearly empty) derived from p_z orbitals. The graphite unit cell consists of two weakly bonded unit cells of the graphene as explained in Sec. 3.1. Thus, the band structure of graphite can be approximated by weakly splitting each graphene band into two as shown below.

The band structure of graphite is plotted along the symmetry lines which define the irreducible wedge of the Brillouin zone (BZ). The first BZ of graphite is drawn in Fig. 4.2. The full zone is reduced to 1/24 due to the symmetry properties of graphite. The high-symmetry points are as labeled on the irreducible part, and their group-theoretical properties[56] are given in Table 4.1.

Q	Symbol	N	The group of k	Order of the group
$(0,0,0)$	Γ	1	D_{6h}	24
$(0,0,1)$	A	1	D_{6h}	24
$(0,0,q_z)$	Δ	2	C_{6v}	12
$(1/3,1,0)$	K	2	D_{3h}	12
$(1/3,1,1)$	H	2	D_{3h}	12
$(1/2,1/2,0)$	M	3	D_{2h}	8
$(1/2,1/2,1)$	L	3	D_{2h}	8
$(1/3,1,q_z)$	P	4	C_{3v}	6
$(1/2,1/2,q_z)$	U	6	C_{2v}	4
$(q_x,q_x,0)$	Λ	6	C_{2v}	4
$(q_x,q_x,1)$	Q	6	C_{2v}	4
$(q_x/2,q_x/2,0)$	Σ	6	C_{2v}	4
$(q_x/2,q_x/2,1)$	R	6	C_{2v}	4
$(q_y/3,q_y,0)$	T	6	C_{2v}	4
$(q_y/3,q_y,1)$	S	6	C_{2v}	4

Table 4.1: The special points and the lines of symmetry in the Brillouin zone of the hexagonal lattice. The wave vector **k** is represented by **Q** according to $[k_x, k_y, k_z] = [(2\pi/a)Q_x, (2\pi/\sqrt{3}a)Q_y, (2\pi/c)Q_z]$, and $0 < q_x < 1$, $1/2 < q_y < 1$, and $0 < q_z < 1$. **N** denotes the number of vectors in the star of **k**.

The calculated band structure of Bernal graphite is illustrated in Fig. 4.3 for the equilibrium value of c. It is clear that σ bands separate into low-energy (bonding, σ) and high-energy (antibonding, σ^*) states with a gap in between. The first unoccupied σ^* band is approximately 6 eV above the highest occupied σ band at Γ point where the gap takes its minimum value. In contrast to that π bands are closer to each other and as well as closer to the Fermi level. For this reason, various phenomena relevant to relatively low energy transfer such as the electronic conduction are mainly characterized by π bands near Fermi level produced by p_z-type orbitals.

The σ-band gap do not allow σ bands to contribute to the density of states in the vicinity of the Fermi level. In contrast, the π and π^* bands have nonzero contribution, and moreover, π and π^* bands join at the K point, causing the band gap to disappear. Thus, graphite is a semimetal, *i.e.* a material with vanishing gap between valance and conductance bands.
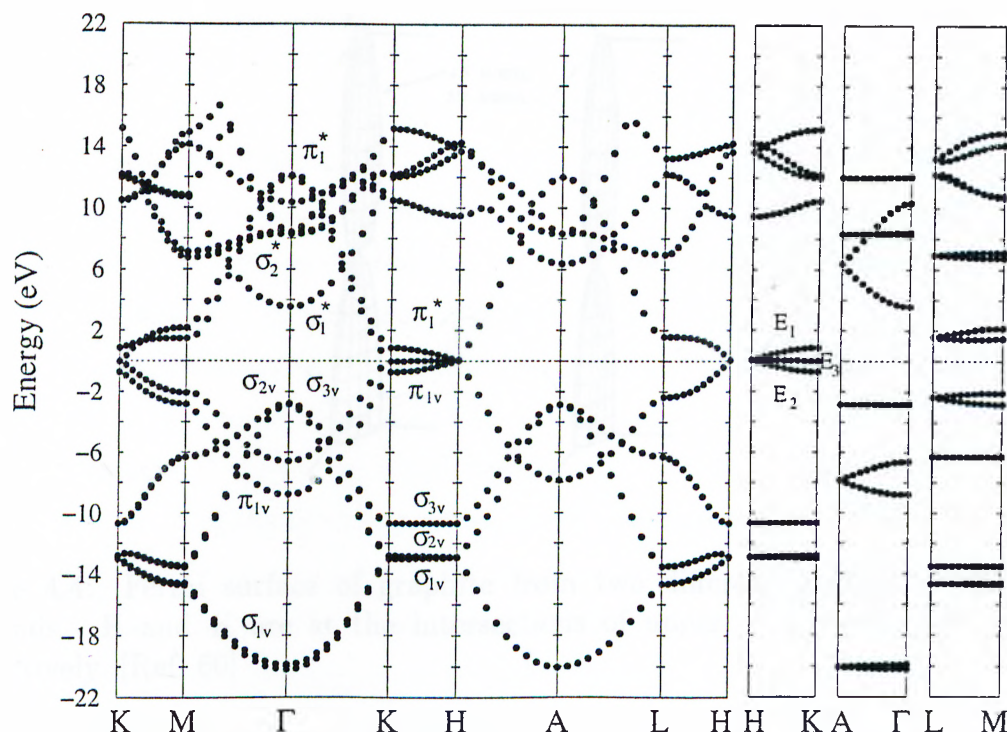
Figure 4.3: Equilibrium band structure of graphite. The zero of energy is taken at Fermi level here and in all figures in this chapter. The occupied bands are labeled by v in subscript. The high-energy states are labeled by $*$ in superscript. σ and π bands are split into two. At Γ point, σ_{1v} represents 1st and 2nd bands, and the others are as follows: π_{1v}: 3rd and 4th bands, σ_{2v}: 5th and 6th bands, σ_{3v}: 7th and 8th bands, σ_1^*: (unoccupied) 9th band, σ_2^*: (unoccupied) 10th and 11th bands, and π_1^*: (unoccupied) 15th and 16th bands.

The Fermi surface (FS) of graphite is usually generated via two interrelated tight-binding models: The Slonczewski-Weiss-McClure (SWMc) model,[57] which is a $\mathbf{k} \cdot \mathbf{p}$ extension of Fermi-level bands near the H-K axis of the Brillouin zone, and the Johnson-Dresselhaus (JD) model,[59] which is based on a full-zone Fourier expansion of π bands, and is equivalent to the SWMc model along the H-K axis. The parameters of these models are determined either from experiments or from *ab initio* calculations. Tatar and Rabii[60] found that Fermi surface is slightly modified when JD model is used instead of SWMc model as seen in Fig. 4.4.
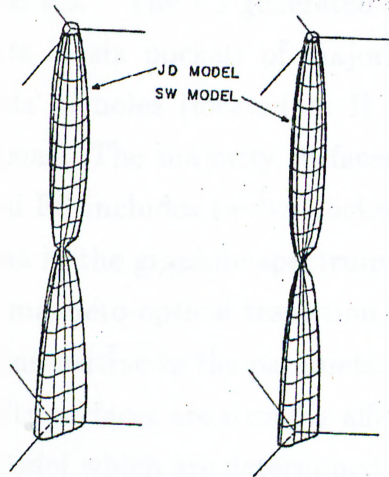
Figure 4.4: Fermi surface of graphite from two different parameterized fits of bands. H and K are at the intersections of upper and lower three axes, respectively. [Ref. 60]

The Kohn-Sham FS within LDA is not necessarily identical to the experimentally determined FS[54]; nevertheless, that of graphite describes the correct location and
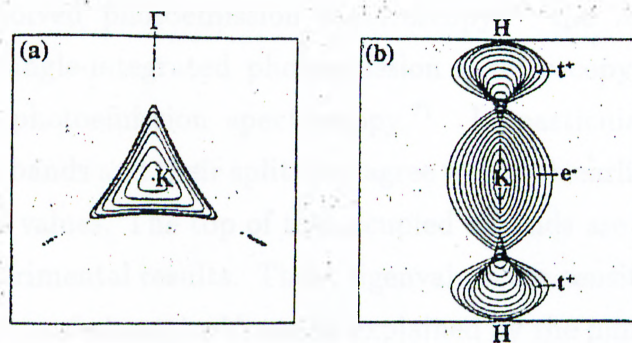
Figure 4.5: Cuts of Fermi surface of graphite through a set of SWMc parameters calculated by *ab initio* techniques. (a) Cuts parallel to $k_x k_y$-plane. (b) Cuts perpendicular to both $k_x k_y$-plane and the K-Γ direction and moved sequentially towards Γ. The contour intervals are 0.06 *a.u.* in (a), and 0.004 *a.u.* in (b). [Ref. 61]

shapes of the experimental FS.[61] The FS generated by SWMc parameterization of LDA calculation results in six pockets of majority electrons (located at K points) and twelve pockets of holes (located at H points) and eighteen small pockets of minority electrons. The majority surfaces are shown in Fig. 4.5. In addition, the experimental FS includes twelve pockets of minority holes.[13] The additional electron extrema in the graphite spectrum which give rise to minority electrons are observed in magneto-optical transition studies.[58] The existence of the majority surfaces are insensitive to the parameters of the SWMC model. On the other hand, the minority surfaces are strongly affected by the variation of the small parameters of the model which are determined rather inaccurately.

The results obtained in this work are in general agreement with the previous LDA results, and experimental data as presented in Table 4.2 and Table 4.3. The theoretical results are based on both pseudopotential and all-electron calculations. In the former group, the norm-conserving,[61,65] soft-transferable,[62] and ultrasoft[34] pseudopotentials are used. The all-electron calculations include the full-potential, linearized augmented plane-wave calculations,[64] the full-potential, linear muffin-tin-orbital calculations,[66] the full-potential, linear combinations of Gaussian-type orbitals fitting-function calculations.[63] The experimental data are obtained by the angle-resolved photoemission spectroscopy,[67] the infrared reflectance spectra,[68,69] the angle-integrated photoemission spectroscopy,[70] and the angle-resolved inverse photoemission spectroscopy.[71] In particular, the bottom of occupied σ and π bands and their splittings agree well with earlier both theoretical and experimental values. The top of the occupied σ bands are found higher than all LDA and experimental results. These eigenvalues are sensitive to the k-point sampling. The error of about 1 eV can be explained by the number of k-points.[64] The calculated value differs from the earlier LDA values by less than 1 eV; the reason is probably due to the uniform mesh used in this work; it samples the BZ along k_z axis with smaller divisions, for this reason the number of k-points on the planes parallel to $k_x k_y$-plane might be insufficient. The bottom of the first unoccupied σ bands agree with all LDA results in that all are lower than the experimental value. The splittings at K point are among the best LDA results

Band index	Present	Ref. 65	Ref. 61	Ref. 62	Ref. 34	Ref. 64	Ref. 66	Ref. 63
σ_{1v}	-20.19	-20.8	-20.1	-19.6	-19.7	-19.6	-19.2	-19.54
	-19.88	-20.5	-19.8	-19.2	-19.35	-19.3	-19.2	-19.24
π_{1v}	-8.78	-9.1	-8.9	-8.7	-8.8	-8.7	-7.8	-8.59
	-6.6	-7.1	-6.8	-6.6	-6.7	-6.7	-6.4	-6.61
σ_{2v}	-2.87	-3.4	-3.5	-3.0	-3.05	-4.6	-3.4	-3.28
σ_{3v}	-2.79	-3.3	-3.4	-3.0	-3.0	-4.6	-3.4	-3.26
σ_1^*	3.52	3.7	3.7	3.9	3.8	3.8	5.7	3.94
σ_2^*	8.27	9.0	7.9	8.4	8.5	8.3	7.9	8.41
	8.27	9.3	7.9	8.4	8.5	8.4	8.0	8.46
$E_3 - E_2$	0.70	0.7	0.80	0.58			0.57	0.60
$E_1 - E_3$	0.86	0.8	0.86	0.74			0.68	0.73

Table 4.2: The energies of σ and π bands at Γ point relative to the Fermi level and the splittings of π bands at the K point. Compare present results to the previous LDA results. All energies are in eV. E_1, E_2, and E_3 are defined in Fig. 4.3.

that close to experimental data.

Band index	Present	Ref. 67	Ref. 70	Ref. 68	Ref. 69	Ref. 71
σ_{1v}	-20.19	-20.6				
	-19.88					
π_{1v}	-8.78	-9.3 - -8.1				
	-6.6	-8.1 - -6.5	-5.7			
σ_{2v}	-2.87	-5.5 - -4.3				
σ_{3v}	-2.79	-5.5 - -4.3				
σ_1^*	3.52					4.5-5.0
σ_2^*	8.27					9.5-10.0
	8.27					9.5-10.0
$E_3 - E_2$	0.70			0.68	0.74	
$E_1 - E_3$	0.86			0.81	0.88	

Table 4.3: The energies of σ and π bands at Γ point relative to the Fermi level and the splittings of π bands at the K point. Compare present results to the experimental data. All energies are in eV. E_1, E_2, and E_3 are defined in Fig. 4.3.

4.2.1 Effects of Uniaxial Distortions on Band Structure

According to the results of the classical MD simulations, the graphite slab is locally distorted by the tip. Not only the atoms under the tip move towards the adjacent layer but also the layer in the close proximity of the tip become either nearer or farther to the subsurface layer. Hence, the lattice parameter c deviates from the equilibrium value locally; the effect of distortion is examined by changing the interlayer distance under uniaxial strain by keeping the intralayer atomic distance fixed at equilibrium value. It is believed that the screening is not strong due to low electron concentration and hence the local modifications of electronic properties such as LDOS, DOS or band structure can be deduced from uniform deformations. The present calculations show that the metallicity of graphite increases as its layers become closer. There occurs transition from semimetallic phase to metallic phase while graphite is being uniaxially compressed.
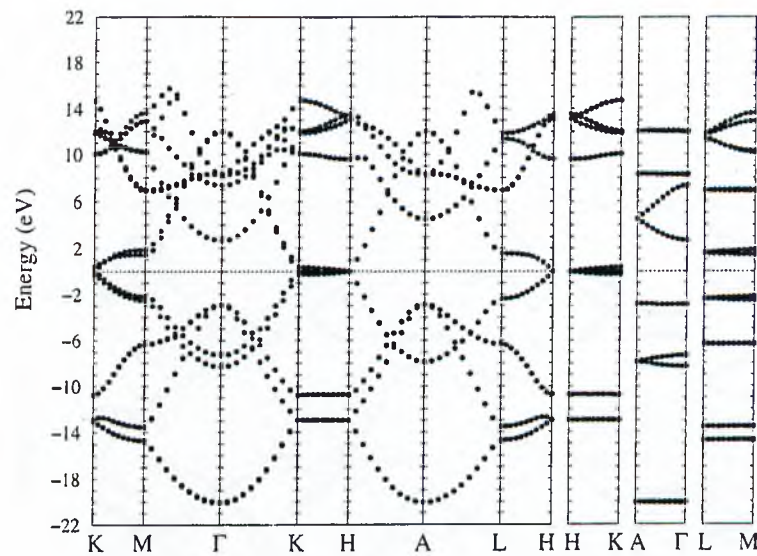

Figure 4.6: Band structure of graphite under uniaxial expansion ($c = 7.674$ Å).

The band structure is calculated for various values of the lattice parameter c, ranging from 4.174 Å to 7.674 Å by an increment of 0.5 Å. Not all but some are presented in Fig. 4.6, Fig. 4.7, and Fig. 4.8. In the case of uniaxial expansion,

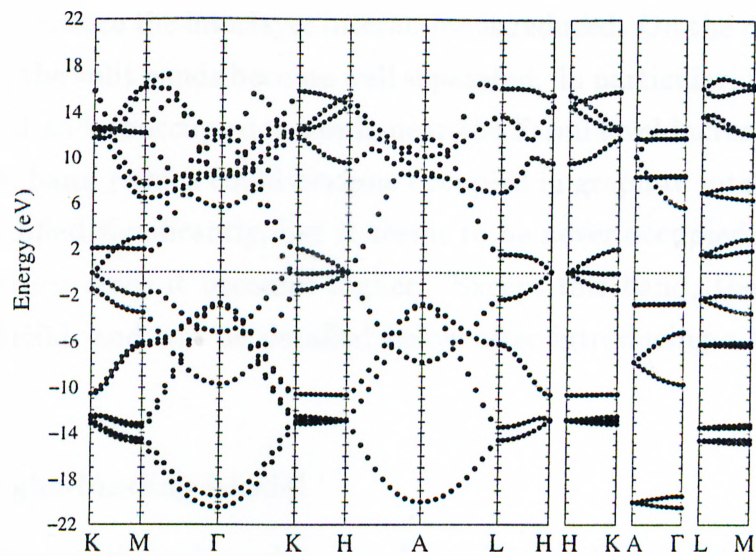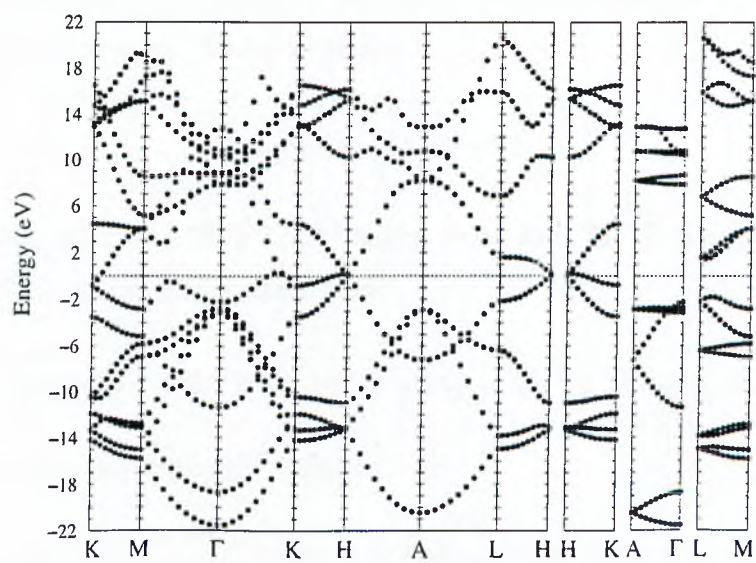Figure 4.7: Band structure of graphite under uniaxial compression ($c = 5.674$ Å).

Figure 4.8: Band structure of graphite under uniaxial compression ($c = 4.674$ Å).

splittings of the bands tend to vanish, and the band structure becomes similar to that of graphene since the interlayer interaction is reduced. On the other hand, as c gets smaller, the split bands become well separated. In particular, the dispersion of the occupied and unoccupied π bands near the Fermi level increases. The first unoccupied σ^* band (which could become occupied in graphite intercalated with metals) is modified significantly, but it seems to be never occupied. The σ-band gap also increases since it becomes higher. Except this band, the variation of π bands is crucial, and will be detailed below after introducing a tight-binding model.

A Simple Tight-binding Model

The electronic properties of graphite can be represented by the four interacting π bands consisting of only p_z orbitals. Hence, it is possible to construct efficient tight-binding (TB) models via Bloch sum of the p_z orbitals. Two well-known orthogonal models were mentioned before. McKinnon and Choy[72] showed that the forth-nearest-neighbor SWMc model is equivalent to a nearest-neighbor non-orthogonal TB model. A similar model is introduced here to interpret the effect of increasing the overlap between p_z orbitals of adjacent layers. The p_z orbitals are assumed to be single-ζ Slater orbitals:

$$\psi_{p_z}(\mathbf{r}) = \sqrt{\frac{\zeta^5}{\pi}} z e^{-\zeta r}, \qquad (4.1)$$

where the exponent $\zeta = 1.5679$ $a.u.^{-1}$ taken from Ref. 73. The overlap of $\psi_{p_z}(\mathbf{r})$ and $\psi_{p_z}(\mathbf{r} - \mathbf{R})$ is analytically evaluated;

$$S_{p_z}(\mathbf{R}) = \frac{e^{-\zeta R}}{15}[(\zeta^3 R^3 + 6\zeta^2 R^2 + 15\zeta R + 15) - Z^2 \zeta^2 (\zeta^2 R^2 + 3\zeta R + 3)], \quad (4.2)$$

and the two-center parameters[74] follow:

$$
\begin{aligned}
S_{pp\sigma}(R) &= \frac{e^{-\zeta R}}{15}(-\zeta^4 R^4 - 2\zeta^3 R^3 + 4\zeta^2 R^2 + 15\zeta R + 15), \\
S_{pp\pi}(R) &= \frac{e^{-\zeta R}}{15}(\zeta^3 R^3 + 6\zeta^2 R^2 + 15\zeta R + 15).
\end{aligned}
\qquad (4.3)
$$

The Hamiltonian and the overlap matrix are 4×4 matrices whose rows and columns are ordered according to β, α, β', and α' atoms. The following k-dependent matrix elements are derived in terms of the two-center overlaps:

$$
\begin{aligned}
S_{\beta\beta}(\mathbf{k}) &= 1 + 2S_{pp\sigma}(c)\cos k_z c \\
&+ 2S_{pp\pi}(a)[\cos(k_x + \sqrt{3}k_y)\frac{a}{2} + \cos(k_x - \sqrt{3}k_y)\frac{a}{2} + \cos k_x a]
\end{aligned}
$$

$$
S_{\beta\alpha}(\mathbf{k}) = S_{pp\pi}(\frac{a}{\sqrt{3}})[e^{i\frac{a}{2}(k_x + \frac{k_y}{\sqrt{3}})} + e^{i\frac{a}{2}(-k_x + \frac{k_y}{\sqrt{3}})} + e^{i\frac{a}{2}(\frac{-2k_y}{\sqrt{3}})}]
$$

$$
\begin{aligned}
S_{\beta\beta'}(\mathbf{k}) &= \frac{(c/2)^2 S_{pp\sigma}(c/2) + (a/\sqrt{3})^2 S_{pp\pi}(a/\sqrt{3})}{(c/2)^2 + (a/\sqrt{3})^2} \\
&\times 2[e^{i\frac{a}{2}(k_x - \frac{k_y}{\sqrt{3}})} + e^{i\frac{a}{2}(-k_x - \frac{k_y}{\sqrt{3}})} + e^{i\frac{a}{2}(\frac{-2k_y}{\sqrt{3}})}]\cos k_x\frac{c}{2}
\end{aligned}
$$

$$
\begin{aligned}
S_{\beta\alpha'}(\mathbf{k}) &= \frac{(c/2)^2 S_{pp\sigma}(c/2) + (a/\sqrt{3})^2 S_{pp\pi}(a/\sqrt{3})}{(c/2)^2 + (a/\sqrt{3})^2} \\
&\times 2[e^{i\frac{a}{2}(k_x + \frac{k_y}{\sqrt{3}})} + e^{i\frac{a}{2}(-k_x + \frac{k_y}{\sqrt{3}})} + e^{i\frac{a}{2}(\frac{-2k_y}{\sqrt{3}})}]\cos k_x\frac{c}{2}
\end{aligned}
$$

$$
S_{\alpha\alpha'}(\mathbf{k}) = 2S_{pp\sigma}(\frac{c}{2})\cos k_z\frac{c}{2} \tag{4.4}
$$

The matrix elements of Hamiltonian are calculated by the extended Hückel formula[75]:

$$
<\psi_1|H|\psi_2> = K\frac{\epsilon_1 + \epsilon_2}{2} <\psi_1|\psi_2>, \tag{4.5}
$$

where the scale factor $K = 2.1$ as suggested in Ref. 76. All diagonal elements of the Hamiltonian are assumed to be equal, and calculated from the diagonal elements of the overlap matrix:

$$
H_{\beta\beta}(\mathbf{k}) = \epsilon_p[1 + K(S_{\beta\beta} - 1)] \tag{4.6}
$$

where the on-site energy ϵ_p is taken as the Herman-Skillman[77] value for carbon. The off-diagonal elements are of the following form

$$
H_{\beta\alpha}(\mathbf{k}) = \epsilon_p K S_{\beta\alpha}(\mathbf{k}) \tag{4.7}
$$

In this model, all interactions defined between the atoms in the unit cell are taken into account inspite of the fact that some of them are negligible.

The calculated band structure are illustrated in Fig. 4.9 for various values of c which are of interest. The dispersion of each band is similar to that of *ab initio* π bands drawn in Fig. 4.10. However, in the equilibrium band structure splittings at M are almost twice the *ab initio* values. Although this model is inaccurate, it is able to describe the variation of π bands qualitatively.

In a tight-binding study, it is possible to investigate the influence of certain interactions on the band structure separately. This simple tight-binding model confirms that the important changes arise from the increase of the overlap between p_z orbitals of two adjacent layer as the layers approach to each other. The dispersive bands along KH axis (or along k_z direction) arise from $pp\sigma$-type interaction (in notation of the two-center approximation) of α and α' atoms, whereas nearly flat bands arises from the same type interaction between two distant β atoms. The bands are labeled by α and β in subscripts, respectively; the high-energy bands (produced by antibonding states) are labeled by $*$ in
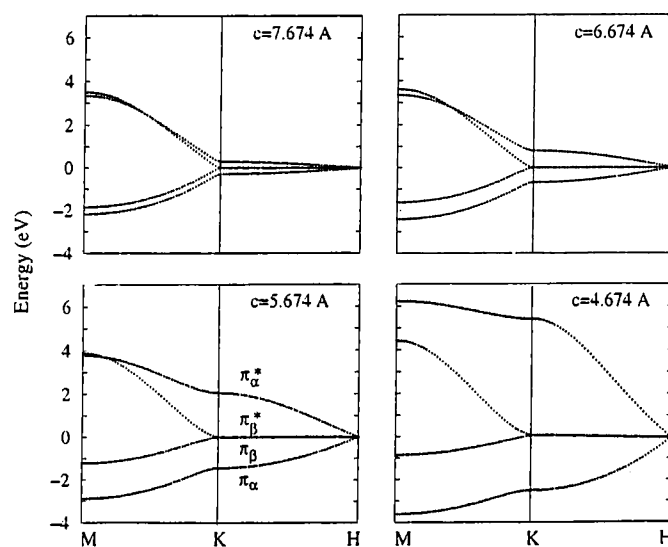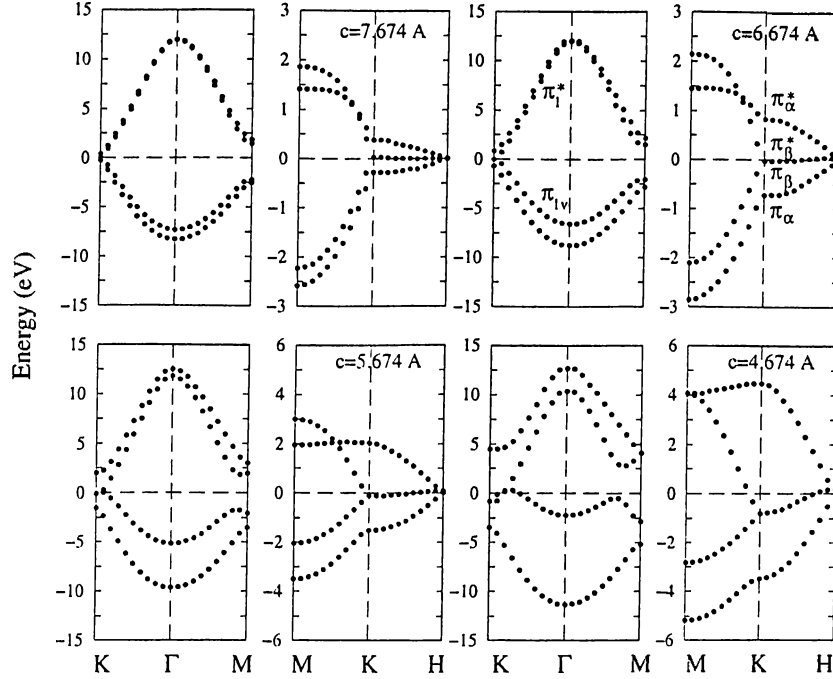

Figure 4.9: TB π bands.

Figure 4.10: *Ab initio* π bands.

superscript. At equilibrium, $pp\sigma$-type (interlayer) integrals are smaller than $pp\pi$-type (intralayer) integrals. As c decreases, $pp\sigma$-type becomes pronounced leading to changes in band dispersion. In this way, the dispersion of π_α and π_α^* increases as graphite is compressed.

Fermi Surface

The variations in Fermi surface can be followed qualitatively from the changes in the band structure. For this purpose, the band structure is detailed near the Fermi level in Fig. 4.11. How the size of the electron and hole pockets of the Fermi surface change is clarified in certain directions: First of all, HKH distance is longer for a smaller value of c. The variation in KH direction is clear in Fig. 4.11: Both the (majority) electron and hole pockets elongates, and the elongation of the electron pocket dominates. In the directions HA and HL, almost no qualitative change is seen in π bands. Hence the majority hole pocket remains approximately

the same in these directions. The directions $K\Gamma$ and KM is not trivial. In the equilibrium band structure, π_1 is fully occupied, and π_1^* is nearly unoccupied, but not completely. For this reason, the very narrow FS is located at K. As c becomes smaller, the occupation of π_1^* increases while that of π_1 decreases. Therefore, an enlargement is expected to be seen in the majority electron pocket because the occupied part of the π_1^* band extends towards Γ and M. On the other hand, the unoccupied part of the π_1 band causes new minority electron pockets to form. The enlargement of the FS is a clear evidence for the increase of metallic properties. On the contrary, as c becomes longer than the equilibrium value the FS becomes narrower. In the limit of infinite interlayer spacing, FS collapses to a point, and the material tend to be a zero-gap two-dimensional semiconductor.
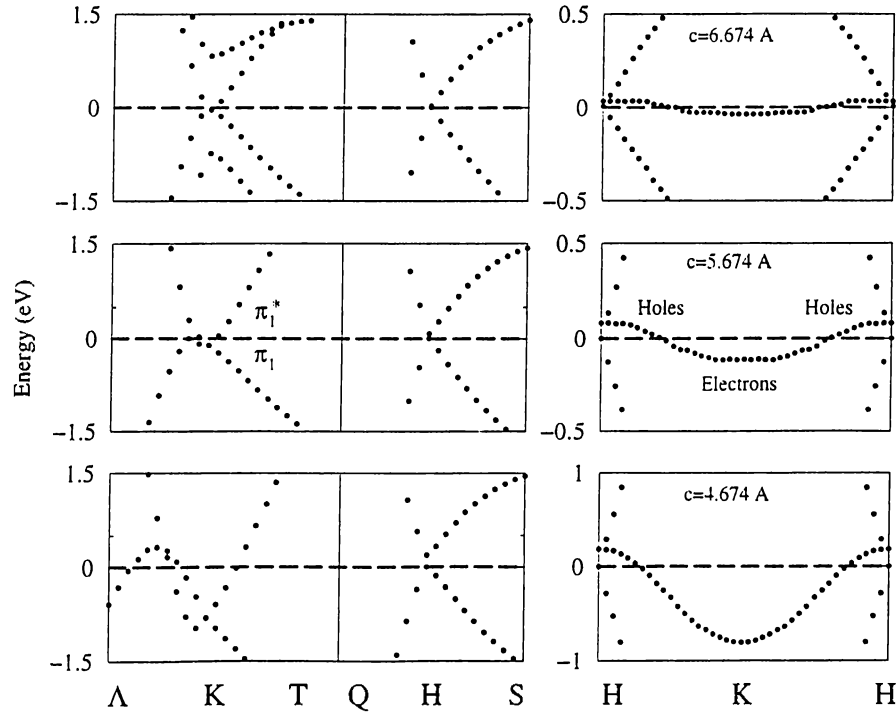

Figure 4.11: Band Structure detailed around Fermi level. The directions $\Lambda(\Gamma K)$, $T(MK)$, $Q(AH)$, and $S(LH)$ denote here the mid-points between two high-symmetry points.

Total Density of States

Metallic properties of graphite is due to very small overlapping of the electron and hole density of states near the Fermi energy. With this small overlap there appears no gap in the vicinity of Fermi level. Since the total density of states (TDOS) at the Fermi level $D(E_F)$ is small, graphite is considered to be a semimetal. The band structure calculations for different values of the interlayer spacing reveals that π bands become more effective in determining electronic properties as c decreases. Therefore, increase of metallicity of graphite is predicted according to the qualitative variations of the Fermi surface. Here, this prediction is proved by TDOS calculations.

The TDOS of graphite is calculated for various values of the lattice parameter c. Three planes of 66 k points (198 points in total) in the irreducible wedge of the BZ are used for this calculation. The energy cutoff is the same as in the band calculations. The calculated TDOS curve is broadened by 0.5 eV Gaussian convolution. The results are presented in Fig. 4.12. It is seen that $D(E_F)$ decreases slightly under small uniaxial strain. In contrast to that $D(E_F)$ exhibits a significant increase when the layers are pressed by uniaxial compressive strain. In Fig. 4.13, the density of states for valance band is compared to the experimental DOS obtained from x-ray photoemission spectroscopy with energetic photons of 122 eV.[70] The experimental broadening is estimated at 0.4 eV. The locations of peaks and dips are nearly the same in both curves whereas the amplitudes are higher in calculated curve.

In conclusion, dramatic changes in metallicity of graphite does not occur under the uniaxial expansion. On the other hand, significant increase is expected in conductivity while graphite is compressed.
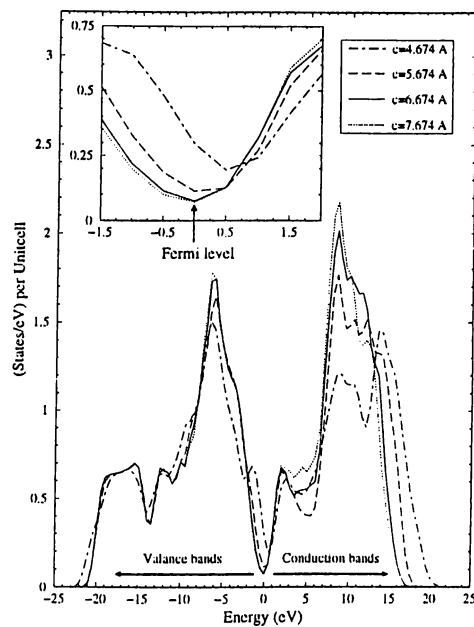
Figure 4.12: Change in the total density of states (TDOS) with respect to variations of lattice parameter c. In the inset, the vicinity of the Fermi level is detailed. In analogy with semiconductors, the energy range is schematically divided into valance and conduction bands regions.
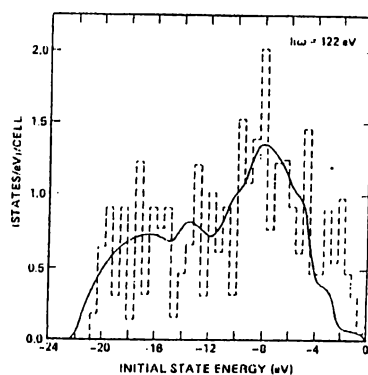

Figure 4.13: The valance band density of states from the experimental x-ray photoemission spectra. The dashed curve is the theoretical density of states. [Ref. 70].

Chapter 5

CONCLUSION

It was revealed by the experiments of two independent groups[11,12] that the two-probe conductance has been observed to change between two values instead of steadily rising, while the tip were continuously pushing towards the graphite surface. However, the results of the experiments were not published for lack of explanation; the behavior was found peculiar in the view of the experience gained from the metal samples. We are not aware of any existing literature, to date, to explain this peculiar behavior. The results of the MD simulations and the electronic structure calculations enable us to propose a new mechanism for the electron transport through a contact formed by a sharp metal tip on the graphite surface. The mechanism proposed in this study provides an explanation of the conductance variation come to exist.

Since the hard tip in the experiments makes long displacements, it presumably punctures the graphite surface in the close proximity of the apex. This event was investigated in our MD simulations. In addition, we observed the destruction of the graphite surface by dislocation-induced crashes following the enlargement of the puncture. It is important to note that the tip apex yet was not proximate to the subsurface. The destruction of the graphite surface do not give rise to much experimental difficulty in obtaining atomic resolution.[78] In the view of this fact, Pethica[79] discussed the existence of graphite flakes, and Abraham and Batra[80] have proposed an explanation of the variety of the AFM (atomic force

microscopy) images of graphite by assuming that the tip is dragging a flake of graphite as it scans the surface. Our results provide evidences supporting their proposal. Since atomic forces are expected to be larger on the STM tip, the existence of such flakes are likely during usual STM scans with a sharp and hard tip at typical imaging conditions ($I \simeq 1\ nA$ and $V \simeq 1\ mV$) under which the physical contact of the tip with the surface is almost inevitable because of small density of states of graphite at the Fermi level.

Three features are important in our atomistic simulations: As the hard tip is approaching the graphite, the top atomic plane is first attracted upwards, later is pressed downwards and the interplanar distance is reduced locally, eventually it is punctured releasing the strain but leaving the apex of the tip freely dipped in the interlayer region. Depending on the shape of the tip and its position on the graphite surface, the puncture occurs either as a local plastic deformation or as a local breaking of the graphite surface into flakes. As the tip is pushed further, the above sequence of events repeats. The effect of the above local deformation induced by a hard tip pressing towards graphite surface was explored by the SCF pseudopotential electronic energy calculations. The density of states at the Fermi level $D(E_F)$ (illustrated in Fig. 4.12) summarizes the effects of the deformations. It is seen that as c decrease, $D(E_F)$ increases; $D(E_F)$ is increased three times by decreasing the interlayer spacing by $\sim 1\overset{\circ}{A}$. This is very important feature that influences the electron transport and plays a crucial role in determining the variation of $G(s)$ curve. A rigorous calculation of $G(s)$ curve for a graphite contact is rather tedious. It requires the knowledge of the self-consistent potential as well as the electronic wave functions quantized at the close proximity of the contact. Neither the model calculations used for normal metals, such as nearly free electron model, nor tight-binding method would give precise results. By combining the results of atomistic simulations of contact and the density of states calculations, we nevertheless propose a mechanism to reveal the physics underlying the peculiar behavior of the conductance through a contact on graphite surface. Owing to the low $D(E_F)$, the opening of the first ballistic channel may not occur for a sharp tip. At the initial stage of the contact, $D(E_F)$ is even lower than that

of the bulk graphite since the surface atoms are attracted by the tip and hence the interlayer distance is slightly increased. As the tip is continued to press the graphite surface, the interlayer spacing decreases locally and consequently $D(E_F)$ of the region where the electrons are transferred increases. Since the current can be given by the expression:

$$I \propto \int_{E_F}^{E_F + e\Delta V} dE D(E) T(E) \tag{5.1}$$

with T being the transmission coefficient, the conductance gradually increases with increasing s until the apex makes a hole on the surface. Once the atomic plane is punctured by the tip, the compressive plane is released and $D(E_F)$ is decreased back to its low value. In the mean time, the apex is plunged into the interplanar region, and I and hence G under constant bias voltage is decreased abruptly. Here we assume that the current from the tip to the punctured layer is negligible. As the tip approaches to a new graphitic plane, the same sequence of events (which has occurred for the first plane) repeats and G varies quasi-periodically with s. Beyond this ideal model, some irregularities can be superimposed on the periodic variations of $G(s)$ owing to the interaction between the tip and the punctured surface atoms. For example, depending on the shape of the tip the residual strain and the average value of the conductance can also increase due to the increased diffusive conductance from the lateral planes. We finally note that for a blunt tip, the highest value of G can be in the range of $2e^2/h$,[81] but it can fall subsequently due to the deformation explained above.

In summary, in this thesis we investigated the conductance through a contact created by an STM tip pushed on graphite surface. The atomistic simulations based on the molecular dynamics method indicate that the growth of the contact on the graphite surface is rather different from that on the normal metals. The contact interface on the metal surfaces grows discontinuously each time causing a sudden jump of conductance in the range of $2e^2/h$. Where as in graphite, the interlayer distance first increases, then decreases and eventually is punctured by the tip pressing the surface. This sequence of events repeats more or less for each new graphitic plane the tip approaches. Using the results of electronic

structure calculations of graphite under strain, we proposed a mechanism of electron transport through the contact on graphite that successfully explains the experimental results.

Bibliography

[1] S. Ciraci, in *Tip-surface Interactions in Scanning Tunneling Microscopy and Related Methods*, edited by R. J. Bohm, N. Garcia and H. Rohrer, p113, Kluwer Academic Publishers, Volume 184 (1990).

[2] J. K. Gimzewski and R. Möller, Phys. Rev. B **36**, 1284 (1987).

[3] E. Tekman and S. Ciraci, Phys. Rev. B **43**, 7145 (1991); E. Tekman and S. Ciraci, *ibid.* **39**, 8772 (1989).

[4] T. N. Todorov and A. P. Sutton, Phys. Rev. Lett.**70**,2138 (1993).

[5] U. Landman, W. D. Luedke, N. A. Burnham and R. J. Colton, Science **248**, 454 (1990); U. Landman and W. D. Luedke. J. Vac. Sci. Tech. 9, 414 (1991).

[6] N. Agraït, J. G. Rodrigo and S. Vieria, Phys. Rev. B **47**, 12345 (1993).

[7] J. I. Pascual, J. Mèndez, J. Gòmez-Herrero, A. M. Barò, V. T. Binch and N. Garcia, Phys. Rev. Lett. **71**, 1852 (1993); J. I. Pascual, J. I. Mèndez, J. Gòmez-Herrero, A. M. Barò, N. Garcia, U. Landman, W. D. Luedke, E. N. Bogachek, H. P. Cheng, Science **267**, 1793 (1995).

[8] J. M. Krans, C. J. Müller, N. van der Post, F. R. Postama, A. P. Sutton, T. N. Todorov, and J. M. Ruitenbeek, Phys. Rev. Lett. 74, 2146 (1995).

[9] A. M. Bratkovsky, A. P. Sutton and T. N. Todorov,Phys. Rev. B **52**, 5036 (1995).

53

[10] Yu V. Sharvin, Soviet Physics-JETP **21**, 655 (1965).

[11] A. Oral (unpublished).

[12] J. K. Gimzewski (unpublished).

[13] N. B. Brandt, S. M. Chudinov, and Ya. G. Ponomarev,*Semimetals: 1. Graphite and its Compounds* (North-Holland, Amsterdam, 1988).

[14] R. J. Borg and G. J. Dienes, *The Physical Chemistry of Solids* (Academic Press, San Diego, CA, 1991).

[15] H.-J. Güntherodt and R. Wiesendanger (Eds.), *Scanning Tunneling Microscopy I* (Springer-Verlag, Berlin, New York, 1992).

[16] E. Tekman and S. Ciraci,Phys. Rev. B **40**, 10286 (1989).

[17] R. Wiesendanger, *Scanning Probe Microscopy and Spectroscopy : Methods and Applications* (Cambridge University Press, Cambridge [England], New York,1994).

[18] J. Bardeen, Phys. Rev. Lett.**6**, 57 (1961).

[19] J. Tersoff and D. R. Hamann, Phys.Rev. Lett. **50**.1998 (1983).

[20] S. Ciraci and E. Tekman, Phys. Rev. B **40**, 11969 (1989).

[21] N. D. Lang, Phys. Rev. B **36**, 8173 (1987).

[22] Y. Imry, in *Directions in Condensed Matter Physics: Memorial Volume in Honor of Shang-keng Ma*, edited by G. Grinstein and G. Mazenko (World Scientific, Singapore, 1986).

[23] A. P. Sutton and J. B. Pethica, J. Phys.:Condens. Matter **2**, 5317 (1990).

[24] J. Ferrer, A. Martín-Rodero, and F. Flores, Phys. Rev. B **38**, 10133 (1988).

[25] I. P. Batra, N. Garcia, H. Rohrer, H. Salemink, E. Stall, and S. Ciraci, Surf. Sci. **181**, 126 (1987).

[26] S. Gwo and C. K. Shih, Phys. Rev. B **47**,13059 (1993).

[27] A. Selloni, P. Carnevali, E. Tosatti, and C. D. Chen, Phys. Rev. B **31**, 2602 (1985).

[28] C. M. Soler, A. M. Baro, N. Garcia, and H. Rohrer, Phys. Rev. Lett. **57**, 444 (1986).

[29] J. Tersoff, Phys. Rev. Lett. **57**, 440 (1986).

[30] Y. Baskin and L. Mayer, Phys. Rev. **100**, 544 (195).

[31] D. Sands, *Introduction to Crystallography* (Benjamin-Cummings, Reading, 1969).

[32] D. A. Mcquarrie,*Quantum Chemistry* (University Science Books, Mill Valley, CA, 1983).

[33] D. Tománek and S. G. Louie, Phys. Rev. B **37**,8327 (1988).

[34] J. Furthfüller, J. Hafner, and G. Kresse, Phys. Rev. B **50**, 15606 (1994).

[35] K. Nordlund, J. Keinonen, and T. Mattila, Phys.Rev. Lett. **77**, 699 (1996).

[36] J. Tersoff, Phys. Rev. Lett. **56**, 632 (1986).

[37] J. Tersoff, Phys. Rev. Lett. **61**, 2879 (1988).

[38] J. Tersoff, Phys. Rev. B **37**, 6991 (1988).

[39] J. H. Rose, J. Ferrante, and J. R. Smith, Phys. Rev. Lett. **47**, 675 (1981).

[40] J. H. Rose, J. R. Smith, and J. Ferrante, Phys. Rev. B **28**, 1835, (1983).

[41] G. C. Abell, Phys. Rev. B **31**, 6184 (1985).

[42] L. Pauling, *The Nature of the Chemical Bond*, 3rd. ed. (Cornell University Press, Ithaca, NY, 1960).

[43] M. T. Yin and M. L. Cohen, Phys. Rev. Lett. **50**, 2006 (1983), and Phys. Rev. B **29**, 6996 (1984).

[44] The data sent by K. Nordlund is used by doing another spline interpolation while implementing the potential.

[45] R. Wyckoff, *Crystal Structures* (Interscience, New York, 1948).

[46] D. P. DiVincenzo, E. J. Mele, and N. A. W. Holzwarth, Phys. Rev. B **27**, 2459 (1983).

[47] S. Fahy, S. G. Louie, and M. L. Cohen, Phys. Rev. B **34**, 1191 (1986).

[48] M. P. Allen and D. J. Tildesley, *Computer Simulation of Liquids* (Oxford University Press, New York, 1987).

[49] D. R. Hamann, M. Schlüter, and C. Chiang, Phys. Rev. Lett. **43**, 1494 (1979).

[50] G. B. Bachelet, D. R. Hamann, and M. Schlüter, Phys. Rev. B **26**, 4199 (1982).

[51] D. M. Ceperley and B. J. Alder, Phys. Rev. Lett. **45**, 566 (1980).

[52] J. Ihm, A. Zunger, and M. L. Cohen, J. Phys. C. **12**, 4409 (1979).

[53] P. Hohenberg and W. Kohn, Phys. Rev. **136**, B864 (1964); W. Kohn and L. J. Sham, *ibid.***140**, A1133 (1965).

[54] W. Kohn and P. Vashishta, in *Theory of the Inhomogeneous Electron Gas*, edited by S. Lundqvist and N. H. March (Plenum Press, New York, 1983).

[55] J.-C. Charlier, X. Gonze, and J.-P.Michenaud, Europhys. Lett. **28**, 403 (1994).

[56] G. F. Koster, in *Solid State Physics: Advances in Research and Applications*, edited by F. Seitz, C. Turn bull, and H. Ehrenreich (Academic Press, New York, 1980), Vol. 5.

[57] J. C. Slonczewski and P. R. Weiss, Phys. Rev. **109**, 272 (1958); J. W. McClure, *ibid.* **108**, 612 (1957).

[58] R. E. Doezema, W. R. Datars, H. Schaber, and A. Van Schyndel, Phys. Rev. B **19**, 4224 (1979); D. A. Platts, D. D. L. Chung, and M. S. Dresselhaus, *ibid.* **15**, 1087 (1977).

[59] L. G. Johnson and G. Dresselhaus, Phys. Rev. B **7**, 2275 (1973).

[60] R. C. Tatar and S. Rabii, Phys. Rev. B **25**, 4126 (1982).

[61] J.-C. Charlier, X. Gonze, and J.-P. Michenaud, Phys. Rev. B **43**,4579 (1991).

[62] M. C. Schabel and J. L. Martins, Phys. Rev. B **46**, 7185 (1992).

[63] J. C. Boettger, Phys. Rev. B **55**, 11202 (1997).

[64] H. J. F. Jansen and A. J. Freeman, Phys. Rev. B **35**, 8107 (1987).

[65] N. A. W. Holzwarth, S. G. Louie, and S. Rabii, Phys. Rev. B **26**, 5382 (1982).

[66] R. Ahuja, S. Auluck, J. Trygg, J. M. Wills, O. Eriksson, and B. Johansson, Phys. Rev. B **51**, 4813 (1995).

[67] W. Eberhardt, L. T. McGovern, E. W. Plummer, and J. E. Fisher, Phys. Rev. Lett. **44**, 200 (1980); A. R. Law, J. J. Barry, and H. P. Hughes, Phys. Rev. B **28**, 5332 (1983); D. Marchand, C. Fretigny, M. Lagues, F. Batallan, C. Simon, I. Rsoeman, and R. Pinchaux, *ibid.* **30**, 4788 (1984); T. Takayashi, H. Tokailin, and T. Sawaga, Solid State Commun. **52**, 765 (1984).

[68] M. Hanfland, K. Syassen, and R. Sonnenschein, Pyhs. Rev. B **39**,12598 (1989).

[69] G. Bellodi, A. Borghesi, G. Guizzetti, L. Nosenzo, E. Reguzzoni, and G. Samoggia, Phys. Rev. B **12**, 5951 (1795).

[70] A. Bianconi, S. B. M. Hagström, and R. Z. Bachrach, Phys. Rev. B **16**, 5543 (1977).

[71] Th. Fauster, F. J. Himpsel, J. E. Fisher, and E. W. Plummer, Phys. Rev. Lett. **51**, 430 (1983); Schäfer, M. Schl'uter, and M. Skibowski, Phys. Rev. B **35**, 7663 (1987); F. Maeda, T. Takayashi, H. Ohsawa, S. Suzuki, and H. Suematsu *ibid.* **37**, 4482 91988); R. Claessen, H. Cartensen, and M. Skibowski, *ibid.* **38**, 12582 (1988); I. R. Colins, P. T. Andrews, and A. R. Law, *ibid.* **38**, 13348 (1988).

[72] B. A. McKinnon and T. C. Choy, Phys. Rev. B **52**, 14531 (1995).

[73] E. Clementi and D. L. Raimondi, J. Chem. Phys. **38**.2686 (1963).

[74] J. C. Slater and G. F. Koster,Phys Rev. **94**, 1498 (1954).

[75] W. A. Harrison, *Electronic Structure and Properties of Solids* (Freeman, San Fransisco, 1980).

[76] M. Menon and K. R. Subbaswamy, Phys. Rev. Lett. **67**, 3487 (1991).

[77] F. Herman and S. Skillman, *Atomic Structure Calculations* (Prentise Hall, Englewood Cliffs, N. J., 1963).

[78] C. M. Mate, G. M. McClelland, R. Erlandsson, and S. Chiang, Phys. Rev. Lett. **59**, 1942 (1987).

[79] J. B. Pethica, Phys. Rev. Lett. **57**, 3235 (1986).

[80] F. Abraham and I. Batra, Surf. Sci. **209**, L125 (1989).

[81] O. J. Marti, Ph. D. thesis, Eidgenössische Technische Hochschule, Zürich, 1986 (unpublished).